

PERPENDICULAR MAGNETIC ANISOTROPY MATERIALS FOR REDUCED CURRENT
SWITCHING DEVICES

by

ZEENATH REDDY TADISINA

A DISSERTATION

Submitted in partial fulfillment of the requirements
for the degree of Doctor of Philosophy
in the Department of Metallurgical and Materials Engineering
in the Graduate School of
The University of Alabama

TUSCALOOSA, ALABAMA

2010

Copyright Zeenath Reddy Tadisina 2010
ALL RIGHTS RESERVED

ABSTRACT

Recently, spin-transfer switching of magnetic tunnel junctions (MTJ's) has become a very active area of research. It is theoretically postulated that using perpendicular magnetic anisotropy materials will substantially reduce the critical current density for switching, resulting in lower energy devices, while keeping the thermal stability high. A range of perpendicular anisotropy material systems, including (i) multilayers, (ii) crystalline alloys, and (iii) amorphous alloys have been intensively studied in this dissertation. The surface and bulk anisotropy, damping parameter, and structural properties of these material systems have been investigated. Magnetic tunnel junctions based on some of these perpendicular material schemes have been fabricated, and their transport properties have been measured and related to the anisotropy. We have found several promising approaches to magnetic tunnel junctions utilized in spin-torque transfer random access memory (STT-RAM).

LIST OF ABBREVIATIONS AND SYMBOLS

GMR	Giant magnetoresistance
HDD	Hard disk drive
MRAM	Magnetic random access memory
MTJ	Magnetic tunnel junction
STT	Spin transfer torque
STT-RAM	Spin transfer torque random access memory
PMA	Perpendicular magnetic anisotropy
MR	Magnetoresistance
SQUID	Superconducting quantum interference device
AGM	Alternating gradient magnetometer
FMR	Ferromagnetic resonance
LEAP	local electrode atom probe
PPMS	Physical Property Measurement System
AMR	anisotropic magnetoresistance
CMR	colossal magnetoresistance
BMR	ballistic magnetoresistance
CPP	Current perpendicular to plane
CIP	Current in plane
TMR	Tunneling magnetoresistance
V	Applied voltage

G	Overall conductance
R	Resistance
P	Spin polarization
e	Electron charge
h	Planck's constant
α	Gilbert damping coefficient
η	spin-transfer efficiency factor
H_{eff}	effective magnetic field
M_s	Saturation magnetization
M_r	Remanant magnetization
IETS	Inelastic electron tunneling spectroscopy
α	In-plane rotation angle
ω	Frequency
UVL	Ultra violet lithography
EBL	Electron beam lithography
d	Lattice spacing
k_B	Boltzmann's constant
H	Magnetic field
H_C	Coercivity field
I	Current
J_C	Current density

ACKNOWLEDGEMENTS

I owe my deepest gratitude to many people who have contributed to the evolution of this dissertation. Foremost among them are Dr. Subhadra Gupta, my advisor, whose immeasurable guidance and continuous encouragement helped me throughout this research project. I would like to thank the faculty members Dr. Ramana G. Reddy, Dr. Gregory Thompson, Dr. Tim Mewes, Dr. Patrick LeClair and Dr. Uday Vaidya for serving on my dissertation committee and giving valuable suggestions.

I wish to thank Dr. Alton Highsmith for many enlightening discussions, suggestions, encouragement and help throughout my work on the project. I wish to thank all the UA-MFF members, Anusha Natarajathinam, Billy Clark, and Courtney Guenther, for their help, friendship, support and providing me valuable inputs. It is wonderful to work with such a talented, hard-working, creative and active group.

Financial and technical support for this project came primarily from Grandis Inc., Milpitas, CA, and U.S Department of Defense DARPA-MTO STT-RAM Universal Memory contract.

I would like to acknowledge the financial, academic and technical support by the professors, staff, and graduate students of the Metallurgical and Materials Engineering Department and MINT Center that have helped me during my study at the University of Alabama.

My greatest debt is to my parents for giving me life, for educating me and supporting me throughout my studies.

CONTENTS

ABSTRACT.....	ii
LIST OF ABBREVIATIONS AND SYMBOLS	iii
ACKNOWLEDGEMENTS	v
LIST OF TABLES	ix
LIST OF FIGURES	x
I. Objectives and Outline	1
1.1 Objectives	1
1.2 Dissertation outline	3
II. Literature Review	5
2.1 Introduction.....	5
2.2 Magnetoresistance in ferromagnetic materials	5
2.3 Discovery of giant magnetoresistance (GMR)	6
2.4 Interlayer exchange coupling.....	8
2.5 Direct exchange coupling	9
2.6 Mechanism of GMR	9
2.7 Types of GMR	10
2.8 Tunneling Magnetoresistance (TMR).....	11
2.9 Spin Torque.....	13
2.10 Applications of Spintronics	13
2.10.1 CIP GMR read head sensors	13
2.10.2 TMR read head sensors.....	14

2.10.3	Magnetic random access memory (MRAM)	15
2.10.4	Spin torque switching random access memory (STTRAM)	16
2.11	Major challenges for STT-RAM technology	18
III.	Experimental Techniques	20
3.1	Introduction	20
3.2	Sputter deposition on SFI Shamrock MR/GMR system	21
3.4	Magnetometry	24
3.4.1	Superconducting quantum interference device (SQUID) Magnetometer	24
3.4.2	Alternating gradient magnetometer (AGM)	25
3.4.3	Ferromagnetic resonance (FMR)	27
3.5	Structural Characterization	27
3.5.1	X-ray diffraction/reflectivity (XRD/XRR)	27
3.5.2	Local electrode atom probe (LEAP)	29
3.6	Electrical characterization	29
3.6.1	Transport measurements/physical property measurement system (PPMS)	30
3.7	Device Fabrication	31
3.7.1	Optical lithography	31
3.7.2	E-beam evaporation	33
3.7.3	Ion milling	34
3.7.4	Stepwise planarization process	35
IV.	Co/Ni Multilayers	38
4.1	Introduction	38
4.2	Experimental details	39
4.3	Results and Discussions	39
4.4	Conclusions	45
V.	Co/Pd Multilayers	47

5.1 Introduction.....	47
5.2 Results and discussion	48
5.3 Current Switching.....	53
5.4 Inelastic tunneling spectroscopy (IETS).....	55
5.5 Conclusions.....	59
VI. Crystalline Alloys	60
6.1 Introduction.....	60
6.2 Thickness dependence of PMA in Co ₅₀ Pd ₅₀ alloys	62
6.3 Temperature dependence of PMA in CoPd alloys.....	65
6.4 Seed layer dependence of PMA of CoPd alloy.....	66
6.5 Conclusions.....	66
VII. Rare Earth Transition Metal (RE-TM) Alloys	68
7.1 Introduction.....	68
7.2 Experimental details	69
7.3 Thickness dependence on PMA of TbFeCo	69
7.4 Thickness of CoFeB on TbFeCo	71
7.5 Seed layer and annealing dependence on PMA and Coercivity of TbFeCo.....	72
7.6 Conclusions.....	75
VIII. Conclusions.....	76
IX. References.....	81

LIST OF TABLES

Table 4.1: Summary of M_{eff} , K_u , and α values for Co/Ni multilayer series with and with of CoFeB.	43
Table 6.1: Summary of magnetic properties of $\text{Co}_{50}\text{Pd}_{50}$ samples as a function of thickness.....	64

LIST OF FIGURES

Figure 2.1: First observation of magnetoresistance of three Fe/Cr superlattices at 4.2 K. The current and the applied field are along the same [110] axis in the plane of the layers [5].	7
Figure 2.2: Hysteresis loops measured at 4.2 K for several (001) Fe/ (001) Cr superlattices with applied field along the (110) axis, in the plane of the layers. The number beside each curve represents the thickness of the Cr layers [5].	7
Figure 2.3: (a) Transverse saturation magnetoresistance and (b) saturation field vs thickness of spacer layer for Co/Ru (left) and Co/Cr (right) structures [11].	8
Figure 2.4: Schematic of spin dependent transport in a GMR structure for both parallel and antiparallel configurations.	10
Figure 2.5: Schematic of CPP and CIP GMR geometries.	11
Figure 2.6: Schematic of TMR effect in MTJ (a) ferromagnetic electrodes are aligned parallel and antiparallel configuration. (b) Corresponding resistance vs. magnetic field response [16]...	12
Figure 2.7: Schematic of MRAM architecture [40].	16
Figure 2.8: Comparison of (a) MRAM and (b) STTRAM cell architectures [39].	18
Figure 3.1: Schematic of SFI Shamrock sputtering system in MFF cleanroom.	22
Figure 3.2: Schematic of S-gun cathode assembly in Shamrock sputtering system.....	23
Figure 3.3: Schematic representation of SQUID placed in a magnetic field.....	25
Figure 3.4: Schematic of sample probe in between the AGM electromagnet.	26
Figure 3.5: Schematic of Model 2900 MicroMag™ AGM.	26
Figure 3.6: Schematic of FMR measurement setup.....	27

Figure 3.7: Principle of x-ray diffraction.....	28
Figure 3.8: Photograph of local electrode atom probe (LEAP) housed in UA-CAF.....	29
Figure 3.9: Schematic of the sheet resistance measurement.....	30
Figure 3.10: schematic of the process flow for patterning using optical lithography.....	32
Figure 3.11: Photograph of Karl Suss MA-6 mask aligner housed in UA MFF.	33
Figure 3.12: Denton vacuum e-beam evaporator housed in UA MFF.	34
Figure 3.13: Intelvac ionmill system housed in UA MFF.	35
Figure 4.1. M-H loops of [Co/Ni] _x N multilayers (a) out of plane (b) in-plane.....	40
Figure 4.2: Microwave frequency measurements of [Co(0.3)/Ni(0.6)] _x 8 multilayered sample. (a) microwave frequency vs. resonance field. (b) linewidth Vs microwave frequency.	41
Figure 4.3. M-H loops of [Co/Ni] _x N/CoFeB0.5 multilayers (a) out of plane (b) in-plane	42
Figure 4.4. FMR measurements of [Co (0.3)/Ni (0.6)] _x N multilayered samples (a) without CoFeB and (b) with CoFeB.	42
Figure 4.5: K _u Vs no of multilayers with and without CoFeB.....	43
Figure 4.6. Stress vs number of multilayers (a) Total thickness of Co/Ni is kept constant (b) Co _{0.3} /Ni _{0.6} ratio is kept constant.....	44
Figure 4.7: Structural characterization of [Co(0.3)/Ni(0.6)] _x N multilayered samples. (a) XRD scan of Co/Ni Multilayer (b) LEAP image of sphere mode reconstruction of Co/Ni multilayers. (c) LEAP concentration profile of multilayers.	45
Figure 5.1: Coercivity vs. thickness of Co in Co/Pd multilayers for (a) Co/Pd as-deposited and annealed multilayers deposited below MgO barrier layer, and (b) Co/Pd as-deposited and annealed multilayers deposited above MgO barrier layer.	48

Figure 5.2: Frequency dependent FMR data of Co/Pd Multilayers with the field applied along the out-of-plane direction (a) frequency vs Hres (b) ΔH vs frequency.	49
Figure 5.3: (a) M_{eff} vs thickness of CoFeB deposited on top of [Co0.2/Pd1]*9 multilayers. (b) Damping constant vs thickness of CoFeB deposited on top of [Co0.2/Pd1]*9 multilayers.	50
Figure 5.4: MH loops of pMTJ with Co/Pd ML's as free and reference layers (a) in plane loop and (b) out of plane loop. The MTJ stack is Pd (seed layer)/ (Co0.2/Pd1)9/ CoFeB0.4/ MgO1.6/ CoFeB0.4/(Co0.3/Pd1)4/Ru (cap).	51
Figure 5.5: MR loops of (a) Co/Pd free and pinned layer and (b) Co/Pd pinned and Co/Ni free layer MTJ's at 100K.	52
Figure 5.6: Out-of-plane MH loops of full MTJ stacks (a) Co/Pd free and pinned layer and (b) Co/Pd pinned and Co/Ni free layer MTJ's at 100K.	53
Figure 5.7: out-of-plane M-H loops of [Co0.3/Ni0.6]x4 ML's with Ta/Pt and Ta/Cu seed layers.	53
Figure 5.8: dI/dV versus I for bias field H_b of 1650 Oe, showing transitions from parallel to antiparallel states of free layer.	54
Figure 5.9: Inelastic and elastic tunneling pathways.	56
Figure 5.10: A typical I-V plot as a result of IETS. A slight increase in slope is observed when the voltage is high enough indicating the inelastic tunneling.	57
Figure 5.11: First and second derivatives of I wrt to V . 2nd derivative plot clearly shows the slight change in the slope as a peak.	57
Figure 5.12: Background-corrected IETS spectra compared with compiled literature data, EELS, and a phonon DOS calculation.	58

Figure 6.1. (a) In-plane and (b) out-of-plane M-H loops of $\text{Co}_{50}\text{Pd}_{50}$ alloys as a function of thickness, showing increasing perpendicular magnetic anisotropy with thickness.	63
Figure 6.2: K_u vs. thickness of $\text{Co}_{50}\text{Pd}_{50}$ alloy.....	64
Figure 6.3: XRD pattern of $\text{Co}_{50}\text{Pd}_{50}$ alloy showing fcc (111) orientation with (a) Ta/Pd, (b) Ta/Pt and MgO seed layers respectively.....	65
Figure 6.5: out of plane loops of $\text{Co}_{50}\text{Pd}_{50}$ 35nm alloy, with (a) Ta/Pd, (b) Ta/Pt & (C) MgO seed layers respectively.....	66
Figure 7.1: In-plane and out-of-plane M-H loops of 12nm TbFeCo film.	70
Figure 7.2: In-plane and out-of-plane M-H loops of 36nm TbFeCo film.	70
Figure 7.3: M-H loops of increasing thickness of CoFeB on top of TbFeCo (a) in-plane (b) out-of-plane loops.....	72
Figure 7.4: Out of plane M-H loops of TbFeCo grown on different seed layers.	73
Figure 7.5: Annealing dependence on coercivity of TbFeCo films.....	74
Figure 7.6: out of plane M-H loop of TbFeCo with different seed and cap layers.....	75

I. Objectives and Outline

1.1 Objectives

The major objectives in this dissertation were to investigate and optimize various perpendicular or partially perpendicular materials schemes for use in MgO-based magnetic tunnel junctions for ultimate applications in non-volatile memory devices. To this end, we have investigated three classes of material schemes: (i) perpendicular anisotropy multilayers, (ii) perpendicular anisotropy crystalline alloys (fcc, hcp and $L1_0$), and (iii) amorphous rare earth-transition metal (RE-TM) alloys. These material systems have been extensively characterized both magnetically and structurally, and their surface and bulk anisotropy has been estimated, as has the damping parameter, α , associated with them, the goal being to find a low damping, high anisotropy material scheme which will yield high magnetoresistance tunnel junctions.

“Spintronics” is a term coined by Stuart Wolf of DARPA to describe the world of devices based on the **spin**, rather than the **charge** of the electron, a field that was initiated in 1988 with the discovery of the **giant magnetoresistive effect (GMR)**, and has rapidly gained momentum over the last two decades with quantum leaps achieved in both fundamentals and applications. Spintronics or spin electronics or magnetoelectronics is an exciting field of science and engineering that exploits the magnetic moment associated with the spin of an electron in addition to its fundamental electronic charge in an attempt to build a useful device. These spintronic devices can be much smaller, more versatile and more robust than charge based devices. All spintronic devices work on the simple principle of information storage in electron spins in a particular orientation, either up or down. These spins, being associated with mobile electrons,

carry the information to where it is read or utilized. These spintronic devices are particularly attractive for memory storage and sensor applications because the spin orientation of conduction electrons survives for a relatively long time.

Until recently, the most remarkable success in the field of spintronics has been achieved in read-head sensors which are used in the high-capacity hard disk drives (HDD's). The major spintronic effect involved in these read-head sensors is known as giant magnetoresistance (GMR), which was discovered in the year 1988 independently by groups led by Albert Fert in France and by Peter Grünberg in Germany, for which they received the Nobel Prize in physics in 2007. A typical GMR device consists of at least three layers, of which two are conducting ferromagnetic layers, separated by a conducting non-magnetic spacer, whose resistance depends on the relative orientation of the magnetic layers. The basis of GMR is that, in ferromagnetic materials, the electrons which are near or at the Fermi level are partially spin-polarized. In these multilayers the resistance is smallest (largest) when the magnetizations of the two ferromagnetic layers are parallel (antiparallel). In recent years, research has been progressing on developing more sophisticated spintronic devices. One such device is magnetoresistive random access memory (MRAM) which employs a magnetic tunnel junction (MTJ) as the storage element. A magnetic tunnel junction (MTJ) is similar to a GMR spin valve except that the non-magnetic conductive spacer is replaced by a non-magnetic insulator. One of the major advantages of MRAM is non-volatility, meaning that information is stored even when the power is turned off, potentially providing instant turn-on computing. Other advantages, such as superior switching speed and endurance combined with non-volatility, make it suitable for use as a universal memory. However, due to several disadvantages, primarily high programming currents and scalability issues, MRAM is limited to niche products, such as automotive applications (crash

recorders, automotive sensors) and consumer applications (mobile phones, gaming machines etc). More recently, a new phenomenon in which the magnetization of a thin ferromagnetic film can be switched by direct transfer of angular momentum from a spin polarized current has been theoretically predicted and experimentally confirmed. This phenomenon is called spin transfer torque switching (STT). This phenomenon can address issues related to MRAM such as scalability and high programming currents. Extensive research is ongoing in the spintronics community to find new MTJ materials and structures which can be used in the STT-RAM devices. In this dissertation, we have explored new MTJ materials and structures, mainly the perpendicular magnetic anisotropy (PMA) materials which are theoretically predicted to be the best type of structure for STT-RAM applications.

1.2 Dissertation outline

Chapter two gives a general background and a literature survey covering the theory behind different types of magnetoresistance (MR) effects, as well as reviews of major experimental advances demonstrating these effects. The two most important magnetoresistance effects, 1) giant magnetoresistance (GMR) and 2) tunneling magnetoresistance (TMR) are discussed in detail. The types of GMR and the phenomenon of exchange bias are discussed. Finally, various applications, such as hard disk drives (HDD), magnetoresistive random access memory (MRAM), spin transfer torque random access memory (STT-RAM) and future challenges associated with their use are discussed.

Chapter three describes the experimental techniques used in this dissertation. Thin film deposition using a production-quality planetary sputtering tool, (SFI Shamrock) is discussed. Magnetic characterization techniques utilized include superconducting quantum interference device (SQUID) magnetometry, alternating gradient magnetometry (AGM), and ferromagnetic

resonance (FMR). Structural characterization includes Philips X'Pert x-ray diffraction, x-ray reflectivity and Imago local electrode atom probe (LEAP). Transport measurements were conducted utilizing a Quantum Design Physical Property Measurement System (PPMS). Device fabrication techniques such as photolithography, ion milling, e-beam evaporation and reactive ion etching are described.

In *chapter four* we have systematically studied the perpendicular magnetic anisotropy (PMA) of Co/Ni magnetic multilayers (ML's). The effect of Co and Ni individual thickness ratios Co/Ni ML's has been investigated by magnetic hysteresis loops as well as ferromagnetic resonance measurements. Stress measurements were performed on these as-deposited samples. Finally, structural characterization such as X-ray diffraction and local electrode atom probe analysis were performed to find out the crystallographic orientation of these multilayers and interdiffusion between them.

Chapter five discusses the perpendicular magnetic anisotropy (PMA) optimization of Co/Pd ML's. In particular the effect of bilayer thickness, bilayer ratio and number of bilayers on PMA is discussed. The effect of seed layers such as MgO and Ta/Pt on PMA is also studied. Finally these optimized stacks were deposited as pinned and free layers in MTJ's and fabricated and transport properties were studied.

In *chapter six*, attempts were made to optimize the PMA of L10 alloys. We have studied the effect of different annealing temperatures and seed layers on PMA of CoPd alloy. We have also studied the effect of composition on PMA of this alloy.

In *chapter seven*, attempts were made to optimize the PMA of rare earth transition metal (RE-TM) alloys, culminating with our partial success with the CoPd alloy, which demonstrated clear PMA, but did not have L1₀ crystal structure.

II. Literature Review

2.1 Introduction

Until recently, conventional electronic devices were based on the charge of the electron. Electrons have another important property, spin, which makes each electron behave like a tiny magnet. Attempts to use this fundamental property have given rise to a new, rapidly evolving field known as “Spintronics” an acronym for spin transport electronics. Until recently, the most remarkable success in the field of spintronics has been achieved in read-head sensors which are used in the high-capacity hard disk drives (HDD’s). The spintronic effect that is utilized in these sensors is the giant magnetoresistance effect (GMR). In recent years more sophisticated devices were developed based on spintronics. One such device is magnetoresistive random access memory (MRAM) [1] which is a solid state device utilizing a magnetic tunnel junction (MTJ) as the storage element. In this chapter we will review the basic concepts behind the different mechanisms of magnetoresistance, in particular the giant magnetoresistance, (GMR) and tunnel magnetoresistance (TMR), and also pay particular attention to the devices based on these mechanisms such as magnetoresistive random access memory (MRAM) and spin-transfer-torque random access memory (STT-RAM).

2.2 Magnetoresistance in ferromagnetic materials

A change in electrical conductivity of a magnetic material due to the presence of a magnetic field is often called magnetoresistance (MR). A variety of MR effects are known and their characteristics depend on the material. Namely, MR effects in metallic, semiconducting and insulating materials have different characteristics. Ferromagnetic materials with metallic

conductance exhibit the anisotropic magnetoresistance (AMR) effect [2] that is, the dependence of conductance on the relative angle between the electric current and magnetization. The typical AMR value of the permalloy is about 2-3 % in an applied field of 100 Oe. A number of new structures and materials were discovered which exhibit new kinds of magnetoresistive effects, such as, giant magnetoresistance (GMR), colossal magnetoresistance (CMR) [3] ballistic magnetoresistance (BMR) [4] and tunneling magnetoresistance (TMR). Colossal magnetoresistance (CMR) of more than 150% at room temperature is first observed in manganese based perovskite oxide in 1993. The CMR effect is because of a strong mutual coupling of the spin, charge and lattice degrees of freedom in this material. However, both GMR and TMR have found many applications to date.

2.3 Discovery of giant magnetoresistance (GMR)

Giant magnetoresistance (GMR) was first discovered in 1988 independently by Albert Fert et al.[5] and by Peter Grunberg et al.[6-7] on Fe/Cr/Fe multilayers grown by molecular beam epitaxy (MBE). The Fe layers were antiferromagnetically coupled through a thin Cr spacer layer at zero magnetic field, yielding a high resistance. As the magnetic field was increased, the magnetic layers were aligned parallel, thereby decreasing the resistance as shown in figure 2.1. The magnitude of the change in resistance led them to name this effect as the “giant” magnetoresistance (GMR) effect.

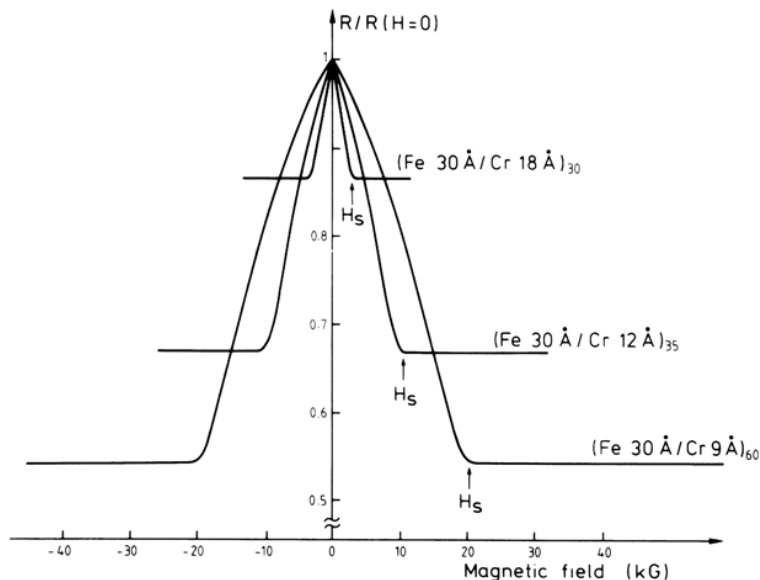


Figure 2.1: First observation of magnetoresistance of three Fe/Cr superlattices at 4.2 K. The current and the applied field are along the same [110] axis in the plane of the layers [5].

They also measured the magnetization of Fe/Cr superlattices and found the antiferromagnetic coupling in adjacent Fe layers when the Cr thickness is lower than 30 Å. A high saturation field of 2T was needed to overcome the antiferromagnetic coupling and saturate the magnetization of the superlattices as shown in figure 2.2 which was correlated to the change in resistance.

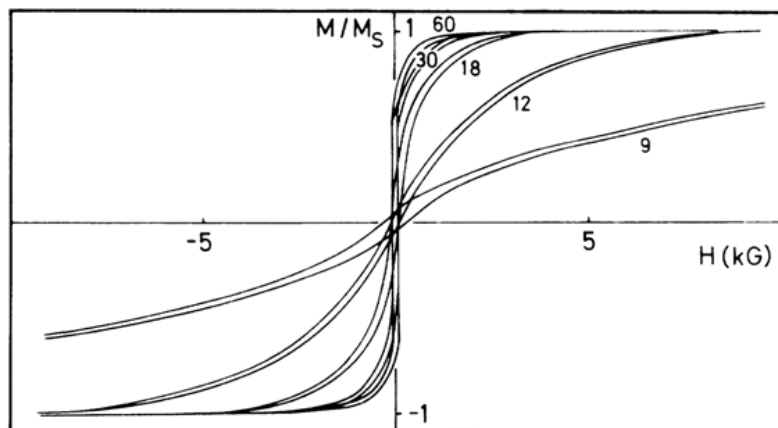


Figure 2.2: Hysteresis loops measured at 4.2 K for several (001) Fe/ (001) Cr superlattices with applied field along the (110) axis, in the plane of the layers. The number beside each curve represents the thickness of the Cr layers [5].

2.4 Interlayer exchange coupling

Later, in 1990, Parkin et al. [8] observed in Fe/Cr polycrystalline superlattice structures that the two ferromagnetic layers could be coupled ferromagnetically or antiferromagnetically at zero magnetic field, based on the thickness of the Cr spacer layer. These polycrystalline superlattice structures were achieved using magnetron sputtering, a relatively straightforward production-worthy process compared with MBE. The magnitude of GMR varied from a finite value to zero, following the oscillating ferromagnetic and antiferromagnetic coupling as the spacer thickness increased. Later it was found by Parkin et al. [9-12] in 1991 that the GMR effect is found in a wide variety of transition metal-magnetic metal multilayers, such as Co/Ru and Co/Cr as shown in figure 2.3.

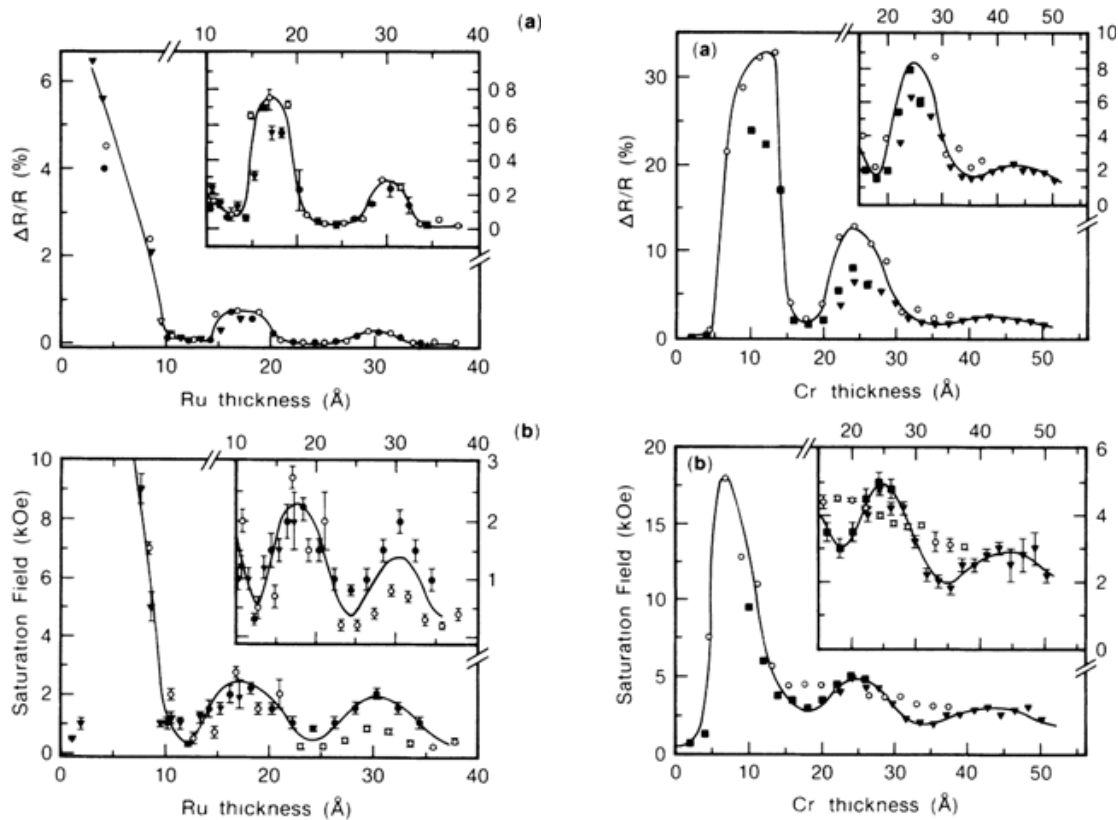


Figure 2.3: (a) Transverse saturation magnetoresistance and (b) saturation field vs thickness of spacer layer for Co/Ru (left) and Co/Cr (right) structures [11].

This oscillation in the GMR value is attributed to the oscillation of the interlayer exchange coupling between the ferromagnetic layers. The coupling oscillated between the negative and positive values of the interlayer exchange coupling constant. The value of the coupling constant is positive for ferromagnetic coupling, where the successive ferromagnetic layers are parallel, and the coupling constant is negative for antiferromagnetic coupling, where the successive ferromagnetic layers are anti parallel in alignment.

2.5 Direct exchange coupling

The phenomenon of direct exchange coupling between the ferromagnet and an antiferromagnet was observed by W.H.Meiklejohn [13-14] in 1956 where in an exchange bias in the hysteresis behavior of the ferromagnetic materials is observed when it is adjacent to a antiferromagnetic material. This led to the discovery of spin valves where a combination of soft and hard magnetic layers was employed. The simplest form of a spin valve structure consists of a soft, ferromagnetic layer, non-magnetic metal spacer layer and a second ferromagnetic layer (pinned layer) exchange coupled by an antiferromagnetic layer (pinning layer). This structure was found to be more useful for technological applications although similar MR values were obtained at zero magnetic fields by superlattice structures. This is because superlattice structures require larger fields to saturate and hence the sensitivity per unit magnetic field is very small.

2.6 Mechanism of GMR

The basic mechanism of GMR is based on understanding the spin dependent transport in ferromagnets as explained by Mott in 1936 [15]. He showed that at low temperature the conductivity in a ferromagnet can be considered as a sum of the two currents arising from the spin up and spin down electrons. This is known as the two current model. The two spin channels of current (spin up and spin down electrons) have different scattering probabilities depending

upon the magnetization of the layer they are traveling through. When a thin layer of nonmagnetic material was sandwiched between two ferromagnetic electrodes as shown in figure 2.4, the resistance of the structure for parallel magnetic moment configuration was found to be low, while the resistance for the antiparallel configuration was high and the change of resistance was expected to be 100% for some quality devices and hence this phenomenon was known as the giant magneto resistance (GMR) effect.

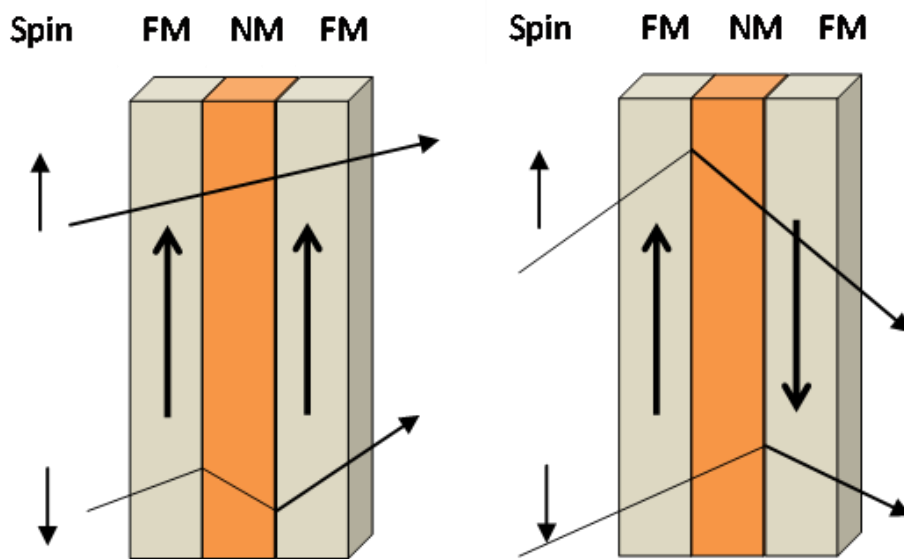


Figure 2.4: Schematic of spin dependent transport in a GMR structure for both parallel and antiparallel configurations.

2.7 Types of GMR

The GMR structures can be divided into two major types: Current in plane (CIP) GMR and Current perpendicular to the plane (CPP) GMR. The type of GMR first observed by the teams led by Fert and Grünberg is CIP GMR. The physics of these two types of GMR are quite different. In CIP GMR current is parallel to the planes of the layered magnetic films, whereas in CPP GMR the electrons have to travel perpendicular to the magnetic layers as shown in figure 2.5.

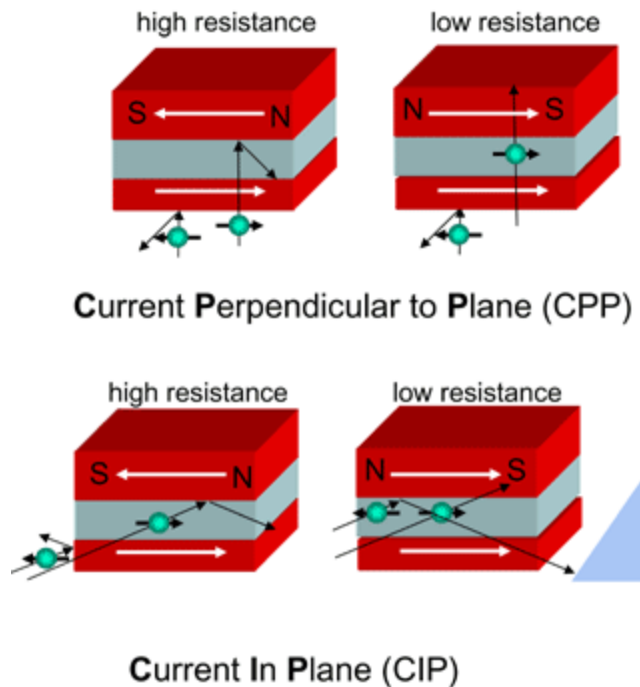


Figure 2.5: Schematic of CPP and CIP GMR geometries.

It is easy to measure the resistance in CIP geometry than in CPP geometry, because in CPP geometry the resistance of the metallic film is usually tiny across its thickness. The thickness of the metallic films in CPP geometry must remain small compared to the distance over which the electrons remember their spin. This distance is usually of the order of one to twenty nanometers in the magnetic materials. So in order to realize a CPP GMR device, the lateral dimensions of the device should be of the order of the thickness of the magnetic layers. Although CPP GMR is very attractive from an application point of view, there are experimental difficulties in fabricating extremely small structures of the order of 10nm.

2.8 Tunneling Magnetoresistance (TMR)

Tunneling magnetoresistance (TMR) is geometrically similar to CPP GMR, the only difference is that the non magnetic metallic spacer is replaced by an insulator and this trilayer structure which consists of a thin insulating layer (a tunnel barrier) sandwiched between two

ferromagnetic metal layers (electrodes) is termed as magnetic tunnel junction (MTJ). The schematic of TMR effect in an MTJ is shown in figure 2.6.

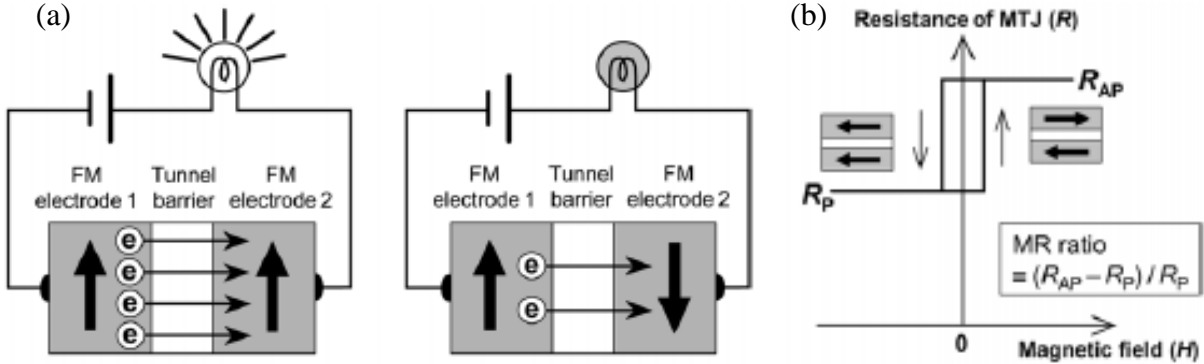


Figure 2.6: Schematic of TMR effect in MTJ (a) ferromagnetic electrodes are aligned parallel and antiparallel configuration. (b) Corresponding resistance vs. magnetic field response [16].

The TMR effect was first observed by Julliere in 1975 [17] where is measured the change in electrical resistance on switching the relative alignment of the Fe and Co magnetic moments from parallel to antiparallel in Fe/Ge-O/Co MTJ structure. The reported change in resistance was 14% at 4.2K. Earlier to his work spin-dependence of tunneling currents through an amorphous aluminum oxide tunnel barrier separating various ferromagnetic electrodes from superconducting aluminum was measured by Tedrow and Meservey. [18-19]. Not much attention was received for the work done by Julliere because the MR ratio was not obtained at room temperature. However after the discovery of GMR his work attracted renewed attention and in 1995 Miyazaki et al [20] and Moodera et al [21] made MTJs with amorphous aluminium oxide (Al-O) tunnel barriers and 3d ferromagnetic electrodes and reported room temperatures TMR ratios as high as 18%. Since these room temperature TMR ratios were higher than the GMR values at that time, the TMR effect attracted a great deal of attention.

In 2001 Professor W. H. Butler, based on first principle calculations predicted that epitaxial MTJ's with a crystalline MgO barrier layer would have MR ratio's over 1000% [22] and later in 2004 two groups [23-24] independently reported TMR ratios of about 200% at RT in MTJ's with a crystalline MgO (001) barrier layer leading to a universal switching over to MgO-based magnetic tunnel junctions (MTJ's) for data storage and other applications. A further discovery by David Djayaprawira [25] utilized amorphous CoFeB electrodes that templated from lattice-matched (001) MgO during the post-deposition annealing process reported even higher TMR values.

2.9 Spin Torque

More recently, a major spintronic phenomenon was predicted independently by John Sloncewski [26] and Luc Berger in 1996 [27] in which the magnetization of a thin ferromagnetic film can be switched by direct transfer of angular momentum from a spin polarized current and this has been experimentally observed [28-30]. In a sense, spin torque phenomenon is the converse of GMR and TMR effects, where the transport of electrons between two ferromagnetic electrodes is affected by the relative alignment of their magnetic moments, as opposed to spin polarized electrons or current causing the magnetic moments to precess in the ferromagnets thereby switching from antiparallel to parallel alignment and vice versa.

2.10 Applications of Spintronics

2.10.1 CIP GMR read head sensors

The first major application of spintronics was CIP GMR spin valve read heads, introduced by IBM in 1996. These devices are used to detect the transitions between the magnetic domains which are used to encode data in hard drives. Information is stored in the form of magnetic bits in the hard drive and the size of the read sensor in the hard drive should be

comparable to the size of the magnetic bit. One of the advantages of the CIP GMR spin valve was that it allowed the sensor to decrease in size, keeping pace with the decreasing size of the magnetic bit in order to increase the storage density. In a CIP GMR spin valve, the magnetization direction of one of the ferromagnetic electrodes, known as the pinned layer, has its magnetic orientation fixed by an adjacent antiferromagnetic layer. The other ferromagnetic electrode (free layer) is free to respond to an external applied magnetic field. When the GMR head passes over a magnetic bit designated as a “0” bit on the disk, it experiences the magnetic field from the “0” bit and the free layer magnetization is aligned with the magnetic field direction from the bit. If the free layer magnetic orientation is parallel to the magnetic orientation of the pinned layer, this results in a lower resistance in the entire head structure. When the head passes over the magnetic field generated from a magnetic bit designated by as a “1” bit on the disk, the magnetic orientation of the free layer rotates so that it is aligned anti-parallel to the magnetization for the pinned layer. This creates a higher resistance in the read head. Therefore, by changes in the resistance of the read head structure caused by the changes in the magnetic orientation of the free layer, magnetic bits in the hard disk drive can be sensed.

2.10.2 TMR read head sensors

More recently, TMR read head sensors have replaced the CIP GMR sensors, due to their large TMR signal as compared to CIP spin valves. Since the current flow in these sensors is perpendicular to structure, it was possible to decrease the size of the magnetic sensor while maintaining a very high signal. However, as bit size continues to decrease, shot noise and high resistance in the smaller TMR sensors may cause problems in future. It is expected that CPP GMR sensors would solve the resistance and shot noise problems in the very small sensor size range, since these use a metallic spacer as opposed to the insulator in TMR sensor. However, the

CPP GMR ratio is still small compared to MgO-based TMR, so newer materials such as half metallic Heusler alloys which have 100% spin polarization play an important role in realizing high GMR ratio CPP sensors.

2.10.3 Magnetic random access memory (MRAM)

TMR is used to read the information stored in a new type of non-volatile memory called magnetic random access memory (MRAM). It has many advantages as compared to the present alternatives; primarily that it is a non volatile memory as compared to conventional dynamic random access memory which requires refreshing of the data. Other advantages include high performance, high density, low power, and high write endurance. A schematic of MRAM architecture is shown in figure 2.7. The information in the form of bits is stored as the relative orientation of the magnetization direction of the two ferromagnetic layers in a magnetic tunnel junction. The higher junction resistance where the two ferromagnetic layers are antiparallel to each other may be assigned as “1” and the lower junction resistance where the two ferromagnetic layers are parallel to each other may be assigned as “0”. These magnetic tunnel junctions are sandwiched between the word and the bit lines which are at right angles to each other. In order to read a particular bit, a current is sent through the bit line passing through the tunnel junction to the ground and by measuring the resulting resistance across the tunnel junction, orientation of the magnetic layers can be determined, which tells us about the present state of the bit. In order to write a bit, a current is sent simultaneously through the appropriate word and the bit lines thereby generating sufficient magnetic field on the bit which is at the intersection of the word and the bit line. The current pulses are selected in such a way that only those cells which are at the cross point of the two lines are switched. All other cells remain unswitched.

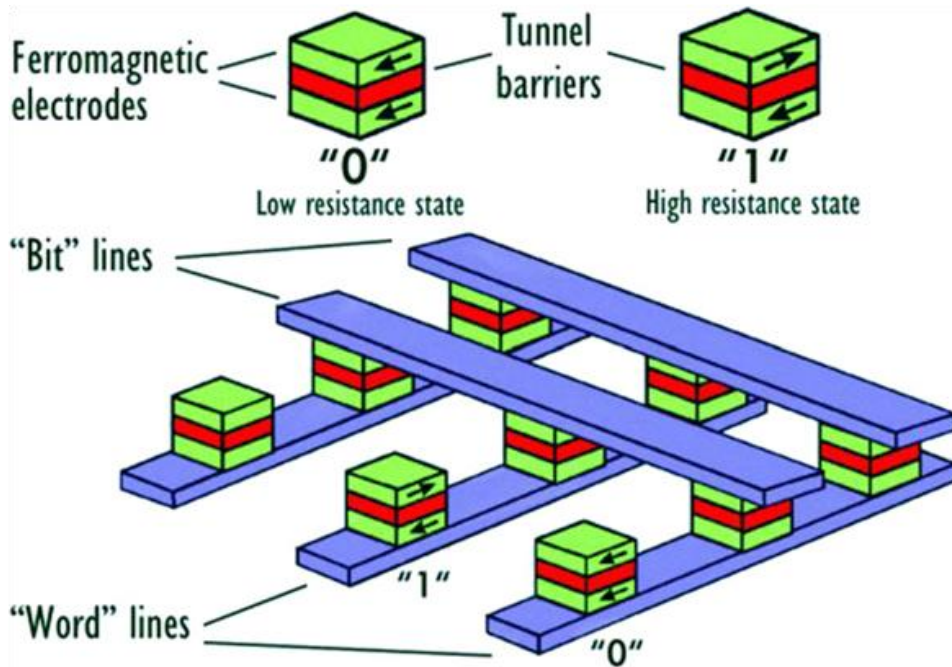


Figure 2.7: Schematic of MRAM architecture [40].

Free scale Semiconductor successfully launched the first commercial MRAM product in 2006. However, as the bit sizes become smaller for higher density MRAM devices, writing becomes a problem, because, as the MTJ size decreases, the free layer is more susceptible to external fluctuations, and hence it is engineered such that it will only switch at higher fields. However, the bit lines which carry the current pulses also need to become smaller, as well as generate enough fields to switch the magnetic layers in the MTJ, leading to overheating problems in bit lines. One solution to this problem is spin torque switching.

2.10.4 Spin torque switching random access memory (STTRAM)

Although MRAM has some potential advantages such as non-volatile memory compared with other technologies, as the size of these devices are shrinking because of the increasing need for high density applications, energy efficient and reliable writing mechanism is critical for realizing a competitive MRAM device. There are two main issues in realizing high density MRAM; first, the programming current is too high because metal lines need to generate a

sufficient magnetic field for the MTJ to switch its storage-layer magnetization. Second, the programming current does not scale down even as the memory cell shrinks. In contrast, STT-RAM devices work favorably if the size of the memory cell decreases. Schematics of cell architectures for MRAM and STT-RAM are shown in figure 2.8. These STT-RAM devices are based on the principle of spin transfer torque wherein the magnetization of a thin ferromagnetic layer can be switched by direct transfer of spin angular momentum from a spin polarized current. For spin-transfer-based MTJ's, the current flowing through the fixed layer polarizes the electrons, these polarized electrons then affect the switching of the free layer, making it parallel or anti-parallel to the fixed layer. The magnitude of this spin transfer effect is dependent on the current density in MTJ's, which is also called the critical current density for switching. It is the total current for switching divided by the area of the element. In other words, critical current density is independent of MTJ size because, the critical current to switch decreases as the MTJ size shrinks thereby keeping the current density constant. This attracted much interest on the STT-RAM devices and with the advancement in fabrication techniques, good quality MTJ's with sizes below 100nm were fabricated, and in late 2005, Sony [31] reported test chip results on a 4kbit STT-RAM device. Later researchers from Hitachi and Tohoku University reported high density STT-RAM devices [32]. However, the critical current density for switching is still too high to realize a high density device.

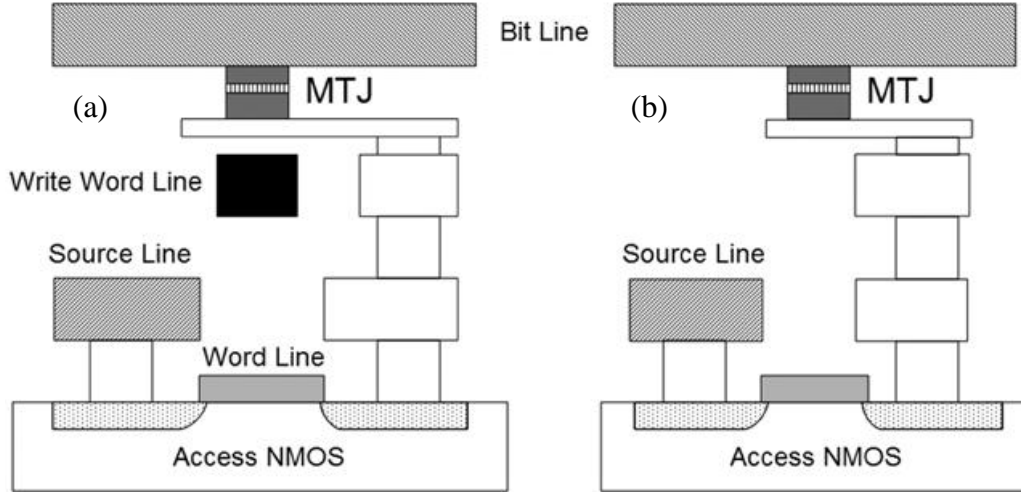


Figure 2.8: Comparison of (a) MRAM and (b) STTRAM cell architectures [39].

2.11 Major challenges for STT-RAM technology

The critical challenge facing STT-RAM technology is to reduce the switching current density J_c of the MTJ used in this device. New materials and structures that may accomplish this have been investigated. It has been theoretically predicted that perpendicular magnetic anisotropy materials (PMA) are advantageous over in-plane anisotropy materials for reducing switching current density in MTJ's used in STT-RAM devices.

The thermal stability factor Δ is given by:

$$\Delta = \frac{K V}{k_B T} \dots\dots\dots (1)$$

Where K = anisotropy constant, V = volume, k_B = Boltzmann's constant and T = absolute temperature.

The critical current, I_c is given by:

$$I_c = \frac{2e}{\hbar} \times \frac{\alpha}{\eta} M_s V \times H_{eff} \dots\dots\dots (2)$$

where α = Gilbert damping coefficient, η = spin-transfer efficiency factor, M_s = saturation magnetization and H_{eff} = effective magnetic field.

For in-plane magnetic anisotropy materials, the effective magnetic field is the sum of the anisotropy field and the demagnetizing field.

$$H_{eff} = H_k + 2\pi M_s \dots\dots\dots (3)$$

For perpendicular anisotropy materials

$$H_{eff} = H_{k\perp} - 4\pi M_s \dots\dots\dots (4)$$

So the above equations clearly show that in-plane magnetic anisotropy materials have to overcome additional demagnetizing fields. So materials with perpendicular magnetic anisotropy are attracting much interest for STT-RAM applications. Recently, perpendicular MTJ's with TMR ratios up to 64% at room temperature were reported using rare earth transition metal (RE-TM) alloys [33-35]. The class of materials known L1₀ alloys have also been extensively studied recently for MTJ applications [36-38].

III. Experimental Techniques

3.1 Introduction

A brief description of experimental techniques and equipment used during the characterization and fabrication of MTJ's is given in this chapter. All the MTJ's were deposited using a production-quality planetary sputtering tool, the SFI Shamrock. Some of the features of this tool, as described below, are unique compared with any other sputtering tool available at UA, resulting in rapid and repeatable generation of complex depositions. Magnetic, structural and transport measurements were performed to characterize the materials and the MTJ devices. Magnetic characterization equipment include: 1) a Quantum Design superconducting quantum interference device (SQUID) magnetometer, 2) an EG&G Princeton alternating gradient magnetometer (AGM), 3) a Digital Measurements System vibrating sample magnetometer (VSM), 4) a SHB B-H looper and 5) an automated broadband ferromagnetic resonance (FMR) set-up custom built by Professor Tim Mewes, all of which instruments are housed in the MINT Center. Structural characterization equipment used include a Philips X'Pert x-ray diffraction and x-ray reflectivity measurement system, JEOL scanning electron microscope, FEI transmission electron microscope, and Imago local electrode atom probe (LEAP), which are all housed in the UA Central Analytical Facility (UA-CAF), with the exception of the Philips XRD system, which is in the MINT Center. Transport measurements were performed on a Quantum Design physical property measurement system (PPMS). Device fabrication was performed using photolithography on a Karl Suss MA-6 mask aligner, ion milling on an Intelvac ion mill,

electron-beam evaporation on a Denton evaporator, and reactive ion etching on an STS Advanced Oxide Etcher, all housed in the UA Microfabrication Facility (UA-MFF).

3.2 Sputter deposition on SFI Shamrock MR/GMR system

Sputtering is a physical vapor deposition (PVD) technique, wherein the material to be deposited is bombarded by high energy ions, there by ejecting the material from the target surface, which is deposited atom by atom onto the substrate. An inert gas such as argon is introduced into the evacuated chamber and is ionized by applying high voltage between the electrodes and generating a glow discharge or plasma.. When a sufficient potential difference is applied between the target material and the substrate, the positive inert gas ions are accelerated towards the surface of the target, knocking out the target atoms, which then condense onto the substrate. The most common types used are DC and RF magnetron sputtering.

Sputter deposition of all the material stacks described in this dissertation was performed on a SFI Shamrock MR/GMR system as shown in figure 3.1. It is a fully automated sputter-up planetary deposition system with seven 3” diameter cathodes (either conical S-guns or planar Sierra cathodes) designed for physical vapor deposition (PVD) of magnetic, non-magnetic and insulating materials. A batch of four substrates up to eight inches in diameter can be run using “one-button” control in “Intouch” mode in less than fifteen minutes. It uses Mystic programmable logic controllers to control and interface the functions of the system to a PC. There is a man-machine interface (MMI) software code which is fully integrated with the Cyrano software which runs the Mystic controllers, which allows direct interfacing with the hardware through the I/O’s. For “one-button” operation, the “InTouch” software mode is used. This is recipe-driven software, and controls the entire sequence of processes run on a cassette of wafers, from loading

the wafers, aligning them in substrate holders (planets) and depositing the whole multilayer stack of materials required to form MTJ's.



Figure 3.1: Schematic of SFI Shamrock sputtering system in MFF cleanroom.

The S-gun cathode has 3 elements of a magnetron, an anode, a cathode and a magnetic field to confine the electrons. An array of permanent magnets are placed around the cathode such that the magnetic flux is parallel to the target surface and intercepts at two corners of the target as shown in the figure 3.2. The magnetron field serves to confine the ions and electrons close to the surface of the target, and they move around the area of heaviest target erosion (the erosion groove or “racetrack”) with a drift velocity proportional to the cross-product of the electric and magnetic fields, and perpendicular to both of them. The cathodes are powered by DC, AC or RF supplies. Reactive deposition of oxides and nitrides may be achieved from elemental targets by sputtering with a given partial pressure of the reactive gas.

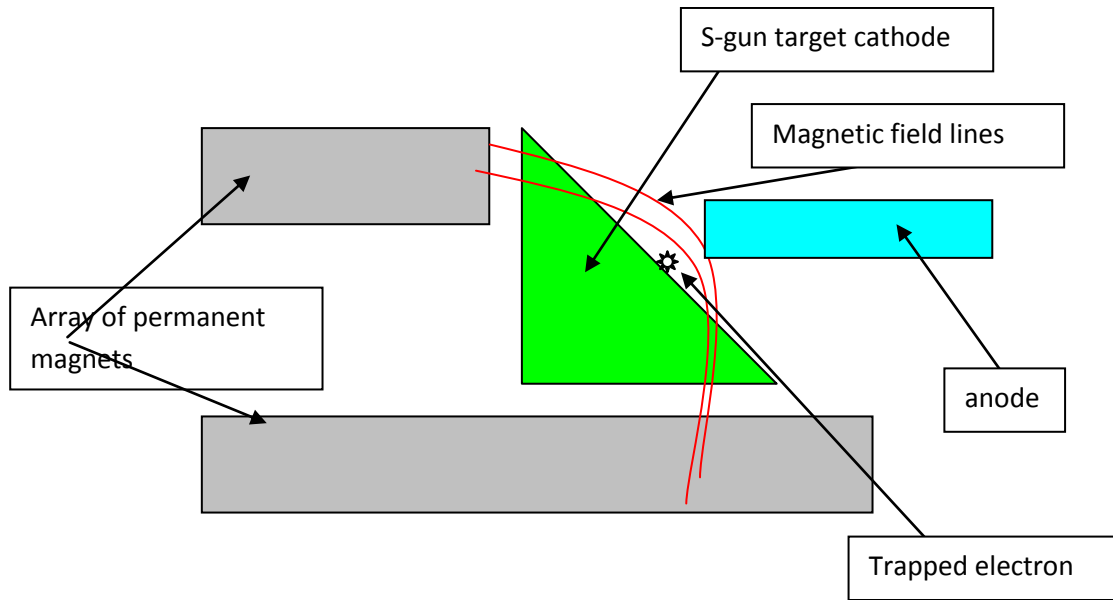


Figure 3.2: Schematic of S-gun cathode assembly in Shamrock sputtering system

The system consists of a cassette module (CM), transfer module (TM) and the sputter module (SM). The cassette module is the loadlock used to load and unload wafers, consisting of a cassette holder which can hold up to 16 6" diameter AlTiC wafers. We used 3" diameter Si wafers or smaller pieces taped to the AlTiC substrates for our experiments. The purpose of the transfer module is to transfer the wafer from the cassette module to the main chamber. A robotic arm picks up the wafer from the cassette module after the alignment is done between the turntable and the aligner for the concerned planet. Once this alignment is confirmed, the wafer is transferred from the cassette module to the sputter chamber by rotating the robot arm by 180 degrees. The allowable speeds for the turntable are 11, 22 and 44 rpm. The sputter chamber is pumped by a turbomolecular pump and a water pump (first stage of a cryopump for removal of water vapor), and is also equipped with bakeout heaters. An overnight pumpdown allows the chamber to reach ultimate base pressures of 9×10^{-9} torr.

The most unique features of the system are:

1. Seven-gun capability, allowing a wide variety of materials to be deposited in one stack.
2. Planetary deposition scheme, providing precise repeatability and resolution of film thicknesses down to 0.1 nm.
3. One-button control, minimizing latency time between layers, thereby minimizing oxidation and yielding high GMR/TMR ratios for all the types of stacks deposited.

The deposition rates for the various materials at different sputtering conditions were determined by depositing fairly thick (over 200 nm) films on glass slides or wafers on which either a permanent marker ink stripe or Kapton tape strip had been applied. The film was removed from the taped or inked region, leaving a sharp profile for thickness measurement. Veeco Instruments Dektak II and Dektak V thin film profilometers were used to measure the thickness of the films. Once sputtering rates were calculated from these thicknesses, the deposition times for the various films deposited under the same power and pressure conditions could be calculated.

3.4 Magnetometry

3.4.1 Superconducting quantum interference device (SQUID) Magnetometer

A Superconducting quantum interference device (SQUID) has the ability to detect very small changes in the applied magnetic flux. These changes can be used to measure any physical quantity related to flux such as magnetic fields, current voltage etc. A SQUID magnetometer consists of superconducting coils or rings with one or two Josephson junctions embedded in it. When a sample is fed into the area enclosed by the ring, the flux change induced due the magnetic sample is detected. A schematic representation of a SQUID placed in a magnetic field is shown in figure 3.3.

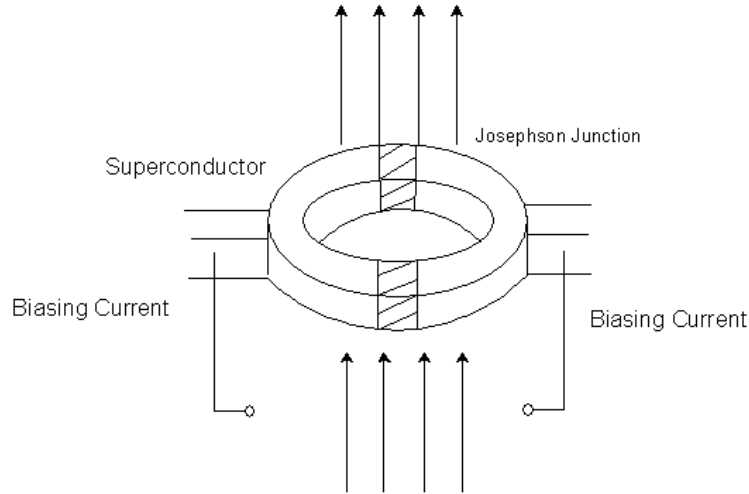


Figure 3.3: Schematic representation of SQUID placed in a magnetic field.

3.4.2 Alternating gradient magnetometer (AGM)

AGM uses an alternating gradient field to produce a periodic force on the sample which is proportional to the gradient field as well as the magnetic moment of the sample. The sample is mounted on an extension rod attached to a piezoelectric element as shown in Figure 3.4. The magnets apply a variable or static D.C magnetic field, H , to change the magnetization of the sample. In addition to the electromagnet, there are four gradient coils which generate an alternative field at the center of the core. This alternating field gradient exerts an alternating force on the sample which is proportional to the magnitude of the gradient field and the magnetic moment of the sample. The sample is deflected because of this alternating force and this change is detected by the piezoelectric sensing element. The output signal from the piezoelectric element is synchronously detected at the operating frequency of the gradient field. The signal developed by the piezoelectric element is greatly enhanced by operating at or near the mechanical resonant frequency of the assembly.

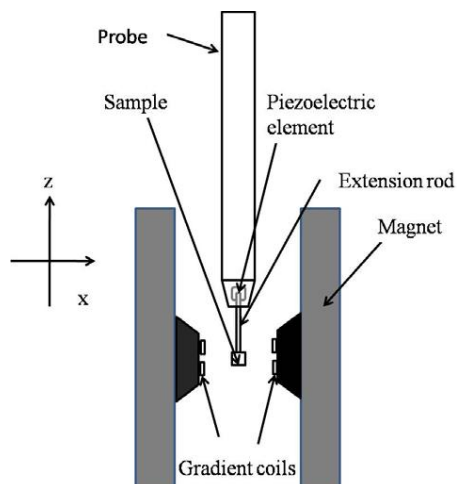


Figure 3.4: Schematic of sample probe in between the AGM electromagnet.

A built-in software function automatically determines mechanical resonance and sets the appropriate operating frequency for the sample under study. Good alignment of the sample is very important for the equipment to find the correct resonant frequency. Model 2900 MicroMag™ AGM has a manual alignment system for one to adjust the sample position along x, y, and z direction as shown in Figure 3.5. The combination of x, y, and z adjustment will finally move the sample to the center of the magnet.

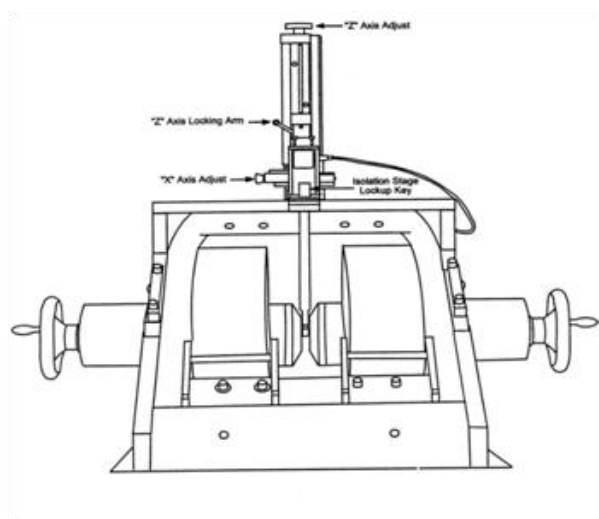


Figure 3.5: Schematic of Model 2900 MicroMag™ AGM.

3.4.3 Ferromagnetic resonance (FMR)

FMR is used to measure magnetic properties by detecting the precessional motion of the magnetization in a ferromagnetic sample. The sample is placed in the microwave resonant cavity which is placed in between the electromagnet. When a static magnetic field H_0 is applied the magnetic moments in the sample precess around the direction of the local field H_{eff} , before relaxation processes damp this precession and the magnetization aligns with H_{eff} . If the sample is irradiated with a transverse rf field (microwaves of typically 1–35 GHz), and if the rf frequency coincides with the precessional frequency, the resonance condition is fulfilled and the microwave power is absorbed by the sample. A schematic of the FMR measurement setup is shown in figure 3.6.

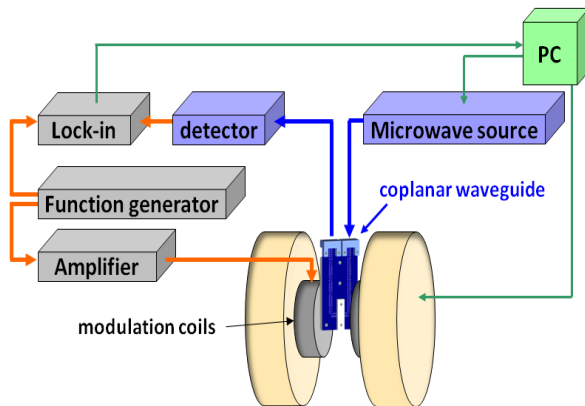


Figure 3.6: Schematic of FMR measurement setup.

3.5 Structural Characterization

3.5.1 X-ray diffraction/reflectivity (XRD/XRR)

The crystalline structure, grain size, thickness of the samples was analyzed by X-ray diffraction on a Philips electronic APD 3600 modified X-ray diffractometer and a Philips X'pert MRD system. This technique is based on observing the scattered intensity of an X-ray beam hitting a sample as a function of incident and scattered angle. The diffraction spectrum follows Bragg's Law which is given by $n\lambda = 2d\sin\theta$, where n is an integer (1, 2, 3, ..., n), λ is the X-ray

wavelength, d is the distance between atomic planes, and θ is the angle of incidence of the x-ray beam striking the sample surface. $2d\sin\theta$ is the path length difference between two incident x-ray beams. This path length difference must be equal to an integer value times the wavelength of the incident x-rays for constructive interference to occur and a diffracted beam is produced. When an x-ray beam encounters the regular, 3-D arrangement of atoms in a crystal most of the x-rays will destructively interfere with each other and cancel each other out, but in some specific directions they constructively interfere and reinforce one another as shown in figure 3.7. It is these reinforced (diffracted) x-rays that produce the characteristic x-ray diffraction patterns that are used to determine the structure of a material.

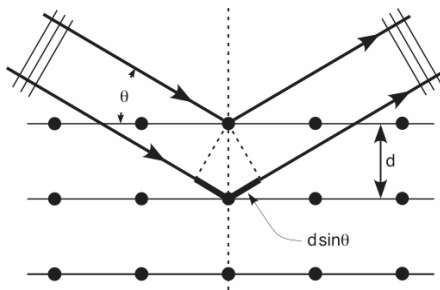


Figure 3.7: Principle of x-ray diffraction.

X-ray reflectivity is a technique used to determine the thickness of a thin film with a very good precision. The refractive index of a material in the x-ray region is given by $n = 1 - \delta + i\beta$, where δ and β represent the dispersion and absorption coefficient of the material. When the incident angle of the x-ray beam is greater than a certain value, known as critical angle (θ_c), it penetrates inside the film. The beam is reflected from the top and bottom surfaces of the film resulting in interference fringes. The path difference $\Delta = m\lambda$ for m^{th} interference maxima is given by $\Delta = 2d\sqrt{\theta_n^2 + 2\delta}$. From XRR measurements, the surface and interface roughness can also be determined.

3.5.2 Local electrode atom probe (LEAP)

LEAP uses the principles of both time-of-flight mass spectroscopy and point-projection microscopy to identify individual elements and to locate them within the bulk of a material and build a 3-D image of sample material. The specimen used for the analysis is a small pointed tip usually $\sim 100\text{nm}$ radius of curvature. These tips can be carved into a wafer using focused ion beam (FIB) processing, or they are also commercially available. The material to be analyzed is then deposited onto these sharp tips. These sharp tips are then inserted into an ultra high vacuum chamber and a positive voltage is applied to the specimen. The positive voltage attracts electrons and results in the creation of positive ions. These ions are repelled from the specimen and pulled toward a position-sensitive detector. The x, y and z coordinates of the ions are then finally mapped in 3D. A photograph of the Imago local electrode atom probe (LEAP), housed in the UA Central Analytical Facility (UA-CAF), is shown in figure 3.8.

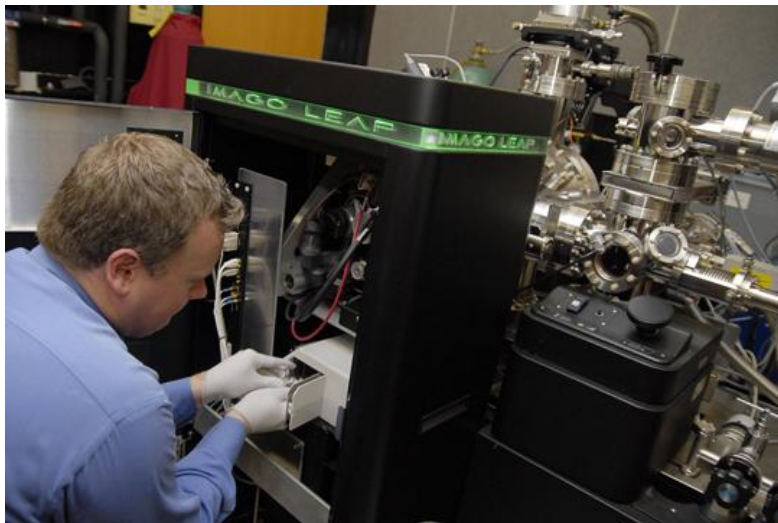


Figure 3.8: Photograph of local electrode atom probe (LEAP) housed in UA-CAF.

3.6 Electrical characterization

Resistivity values of the thin films are usually larger than the bulk samples, this increase in resistivity can be attributed to the interface scattering effects. A standard four point probe was

used to measure the resistance of the thin film samples. A constant current is applied across the sample from the outer two contacts and a voltage drop is picked up from the inner two contacts as shown in the figure 3.9 and the resistance is calculated as

$$\text{Sheet Resistance} = \frac{\text{Voltage}(V)}{\text{Current}(A)} * C_f \quad (C_f = 4.5).$$

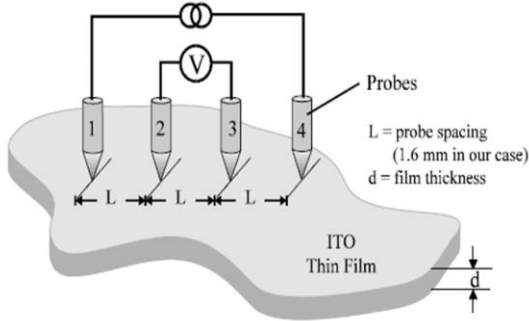


Figure 3.9: Schematic of the sheet resistance measurement.

3.6.1 Transport measurements/physical property measurement system (PPMS)

Magnetoresistance measurements were also done using the four point probe. The sample along with the four point probe set up is placed in the electromagnet. A small amount of current typically of the order of milliamperes is applied to the sample under the influence of the magnetic field. A change in resistance is observed with the sweeping of the applied field, depending on the direction of the two ferromagnetic layers in the spin valve structure. The other magnetic properties, for instance, coercivity, switching field and magnetic saturation values of both the free and pinned layers can also be obtained from these measurements. The magnetoresistance can be obtained from the change in voltage values because of the magnetic field swept with a constant current and it is given by

$$MR\% = \left(\frac{R_H - R_{HS}}{R_{HS}} \right) \times 100$$

where R_H is the resistance at that field and R_{HS} is the resistance at the saturation field. Low temperature MR measurements and thermal stability studies were conducted on a Quantum Design Physical Property Measurement System (PPMS) using liquid helium cooling for measurements at temperatures down to 4.2 K. The Quantum Design Physical Property Measurement System (PPMS) is used for measurement of various physical properties, for instance, heat capacity, magnetometry, electron transport and thermal transport. The sample to be analyzed was placed on the sample “puck” and wired bonded or indium bonded to make the electrical contacts. This puck was connected to a 12-pin connector pre-wired to the system electronics at the bottom of the sample chamber which is vacuum-sealed. This is a very accurate measurement system for studying the temperature dependence of various physical properties from 4.2 K to 400 K with very good precision. A 7 to 16 Tesla longitudinal or 7 Tesla transverse magnetic fields can be used to do magnetometry measurements. The Model P400, for DC resistivity measurements, has four channels that can be used for MR measurements up to three samples in a single sequence. Specifications for this unit include a DC 7.5/8.3 Hz square wave drive with a current range of 5 nA to 5 mA with a step size of 1% of the range or 10 nA, and the current stability is 0.1% over 6 hours from 295 K to 297 K. It has a sensitivity of 20 nV at the compliance voltage of 95 mV and a maximum resistance of 4 M Ω .

3.7 Device Fabrication

3.7.1 Optical lithography

Photolithography is defined as an optical means of transferring patterns on to a substrate. These patterns are first transferred on to a imagable photoresist layer which is a liquid film that is spread on to a substrate. Photoresist is an organic polymer which changes its chemical structure when exposed to ultraviolet light. Photresists can be classified in to two major types based on the

changes in its physical properties when exposed to UV light. In the case of positive photoresist, the part where the underlying material is to be removed is exposed with UV light. The UV light changes the chemical structure of the resist and makes it more soluble in a developer. In the case of negative photoresist, exposure of UV light causes it to become polymerized and more difficult to dissolve. So, the developer solution removes the unexposed part only. A schematic of the process flow for patterning using optical lithography is shown in figure 3.10.

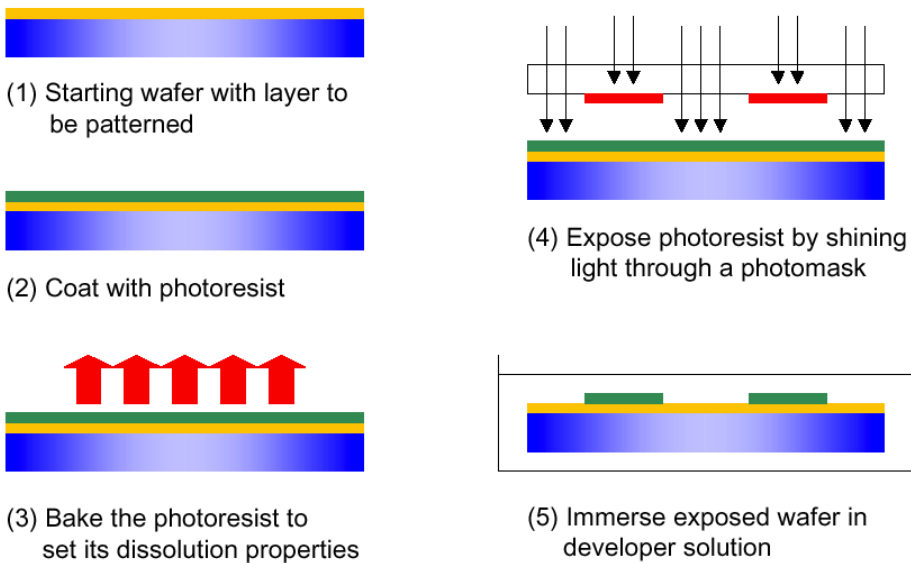


Figure 3.10: schematic of the process flow for patterning using optical lithography.

The major steps involved in patterning using photolithography are wafer cleaning, photoresist application, soft baking, mask alignment, and exposure and development. Figure 3.11 shows the Karl Suss mask aligner which is used in MFF cleanroom.



Figure 3.11: Photograph of Karl Suss MA-6 mask aligner housed in UA MFF.

3.7.2 E-beam evaporation

Evaporation is a physical vapor deposition technique, where in the material to be deposited is loaded in to a heated container, called a crucible, and the material to be evaporated is heated by an intense high energy electron beam which is generated by an electron gun. The beam can be rastered across the material to melt a significant fraction of the surface. This is done by placing a strong magnetic field which bends the incoming electron beam to raster the surface. One of the main disadvantages of e-beam evaporation compared with sputtering is poor step coverage. However, in the fabrication process, poor step coverage helps with the liftoff process, which is why we have used evaporation throughout the stepwise planarization process described in this chapter to deposit silicon dioxide prior to subsequent liftoff patterning. Figure 3.12 shows the Denton Vacuum e-beam evaporator used in the MFF cleanroom. It is used for depositing thin films of metals and dielectrics. It consists of four crucible indexer which permits deposition of up to four different materials without breaking vacuum.



Figure 3.12: Denton vacuum e-beam evaporator housed in UA MFF.

3.7.3 Ion milling

Ion milling is an etch process utilizing an ion source to generate an energetic plasma that strikes the surface of a rotating substrate, milling away the surface material. It is an excellent etch tool for non-reactive metals like gold. Generally, pure ion milling or ion-beam etching uses inert gases such as argon which involves no chemical reactions with the etch materials. It is strictly a mechanical process similar to sandblasting. Ion milling has two major advantages compared to high pressure plasmas; directionality and applicability. The ions in the beams are accelerated by a strong electrical field and the chamber pressure is so low that the atomic collisions are extremely unlikely and hence the milling is directional and also possible for any material since it is chemistry independent. Figure 3.13 shows Intelvac ionmill system used in MFF cleanroom. It can be used to mill wafers up to 4 inch in size and the base pressures obtained in this system are in the range of 2×10^{-7} torr.



Figure 3.13: Intelvac ionmill system housed in UA MFF.

3.7.4 Stepwise planarization process

Our first attempts at producing a spin valve followed very straightforward processing steps – 1) deposit the the bottom electrode and stack, 2) pattern and etch the bottom electrode and stack, 3) pattern and etch the stack to produce a micro-pillar, 4) deposit an insulating layer of SiO₂ over the entire device, 5) pattern and etch a nano-scale opening down to the stack in the SiO₂ atop the micro-pillar, 6) deposit the top electrode, making contact with the micro-pillar at the bottom of the nano-scale opening, 7) pattern and etch the top electrode, and 8) pattern and etch openings through the SiO₂ to the bottom electrode. These earliest efforts to produce a spin valve met with a variety of failures, the most common of which were open circuits and short circuits. The open circuits seemed to arise due to the difficulty of reliably filling the nano-scale hole in the oxide in produced step 5 above during the deposition of the top electrode in step 6. The short circuiting was believed to be the result of poor coverage of the oxide film near any edges, and especially near the edges off the patterned bottom electrode.

To avoid producing opens and shorts, a process methodology was adopted which we have called stepwise planarization. This methodology repeatedly uses a specific sequence of processing steps – pattern, etch, deposit, liftoff – in such a way that the device is kept planar at each critical phase of its fabrication. The critical aspect of this procedure is that the etch depth and the deposition thickness must match, so that the sample will be planar after the liftoff procedure.

Beginning with a thermal oxide coated silicon wafer, the the substrate is patterned with photoresist leaving openings that correspond to the size and shape of the bottom electrodes. This layer of photoresist is used as an etch mask while the thermal oxide layer is etched to a depth corresponding to the thickness of the bottom electrode and stack. After this etch step is complete, the bottom electrode and stack are deposited, filling the holes in the oxide layer. And finally, the photoresist is stripped off of the substrate, lifting the electrode and stack materials off of regions not associated with devices. At the conclusion of this process cycle, the sample is planar, with bottom electrodes and stacks embedded in the thermal oxide layer.

In the next phase of fabrication, photolithography is used to pattern a micron scale feature at the center of each device. This resist layer is used as an etch mask for ion milling through the stack to the bottom electrode, so that the magnetic stack is limited to a pillar protected by the feature of photoresist. After etching, a layer of SiO_2 is deposited via E-beam evaporation. This thickness of this SiO_2 is chosen to match the depth of the pillar etch, so that when the evaporation is complete, the SiO_2 layer is planar with the micro-pillars. After evaporation, stripping of the photoresist lifts off the evaporated oxide from the top of the micro-pillars, leaving us once again with a wafer that is planar.

In case of CPP GMR fabrication, to produce good current confinement, a nanometer scale pillar is etched atop the micron scale pillar described above. E-beam lithography is used to pattern a negative E-beam resist with elliptical “dots”. Ion milling is used to etch down to the spacer layer within the magnetic stack, while the E-beam resist protects the underlying elliptical region. After etching, SiO₂ is deposited via E-beam evaporation to back fill the etched regions with oxide. Finally, the E-beam resist is stripped, lifting off the oxide from atop the nano-pillar, leaving us once again with a planarized wafer.

The last “critical” fabrication step is deposition of the top electrode, but as we are working with a planarized wafer, difficulties in making good contact with the nano-pillar are greatly reduced. A blanket film of top electrode is deposited on the wafer. The wafer is then patterned with photoresist, and ion milled to produce discrete top electrodes. To complete the devices, photolithography is used to pattern “windows” over the bottom electrodes. The oxide layers that have been deposited in prior processing steps are etched away, opening up contacts to the bottom electrodes.

IV. Co/Ni Multilayers

4.1 Introduction

The phenomenon of spin transfer (ST) switching [26, 27&41] wherein a spin polarized current is used to reverse the magnetization orientation of a thin ferromagnetic layer has generated considerable interest in high performance magnetic memory devices. This phenomenon of spin transfer (ST) switching applied to magnetic tunnel junctions with perpendicular magnetic anisotropy (PMA) has generated considerable interest in applications such as spin torque transfer random access memory (STT-RAM) [42]. In order to have high density MRAM, the MTJ cell size should be very small, which works in favor of STT-RAM, because the switching current scales down as the MTJ size shrinks. A low switching current and a large thermal stability factor are the two important issues for realizing high density STT-MRAM. Many approaches to reduce the critical current were investigated [43-46]. The theoretical expressions predict that lower critical currents for switching and high thermal stability can be achieved by using perpendicular magnetic anisotropy materials [42]. This is because the switching current in a perpendicular tunnel junction is proportional to the ratio of effective anisotropy of the free layer to the anisotropy field of the free layer given by H_{eff}/H_k which is equal to 1. However, in the in-plane tunnel junction the switching current has to overcome the additional demagnetizing field term $2\pi M_s$. Thus perpendicular magnetic anisotropy materials have clear advantages over in-plane magnetic anisotropy materials in terms of lower switching currents and high thermal stability factor.

Previous work on optimizing the PMA of Co/Ni multilayers by varying the deposition conditions was carried out in the early 1990's by researchers from Philips Research Laboratories in Eindhoven [47-49]. In this chapter we have studied the perpendicular magnetic anisotropy of Co/Ni multilayer systems as a function of bilayer thickness, bilayer ratio, and number of bilayers.

4.2 Experimental details

A series of Co/Ni multilayers (ML's) were deposited on (100) silicon substrates in a seven-target SFI Shamrock planetary sputtering system using dc magnetron sputtering for all the layers. The sputtering system was pumped down to a base pressure of less than 8×10^{-8} Torr (2.4×10^{-6} Pa). Deposition powers ranged from 250 to 450 W, corresponding to deposition rates of 0.6–1.8 nm/s. Deposition pressures were held at 3 mTorr (0.4 Pa). A combination of Ta/Pt was used as the seed layer to promote the fcc (111) texture of the magnetic multilayers and a capping layer of Ta was used to protect the ML's from oxidation. The magnetic and structural properties of the as deposited samples were measured mainly by alternating gradient magnetometer and X-ray diffractometer. The damping constant α and effective magnetization were measured using a customized, fully automated broadband low temperature ferromagnetic resonance (FMR) capability using coplanar waveguides with a frequency range of 2-70 GHz. Stress measurements were carried out using a Flexus thin film stress tester.

4.3 Results and Discussions

A series of Co(x)/Ni(y) ML's were deposited keeping the total thickness of the stack constant at 7.2 nm to study the PMA. The ratio of $y/x = 2$ is used in all these ML's. It is observed that as the number of ML's is increased, i.e., the individual bilayer thicknesses are decreased, the magnetization of the films goes from in-plane to out-of-plane. Figure 4.1 below shows the M-H

properties of Co/Ni ML's. Here the total thickness of the multilayers is kept constant. As the thickness of the individual layers increases keeping the ratio of Ni/Co = 2, the PMA gradually decreases. It is observed that Co(0.3)/Ni(0.6)x8 ML sample show clear out of plane anisotropy with large H_k field. As the out of plane anisotropy increases the contribution from the demagnetizing fields which tend to keep the film in the plane contribution decreases.

Fig 4.1 (a) shows MH loops of Co/Ni ML's, with field applied normal to film plane. As the total number of ML's decreases from 8 to 4, the coercivity decreases from 160 Oe for 8 ML sample to 65 Oe for 6 ML sample before finally going in-plane for 4 ML with coercivity less than 10 Oe. Fig 4.1 (b) shows MH loops of Co/Ni ML's, with field applied parallel to the film plane. As the number of ML's decreases from 8 to 4, the anisotropy field H_k decreases from 7.5 kOe to 0.5 kOe indicating the decrease in perpendicular magnetic anisotropy of the ML's.

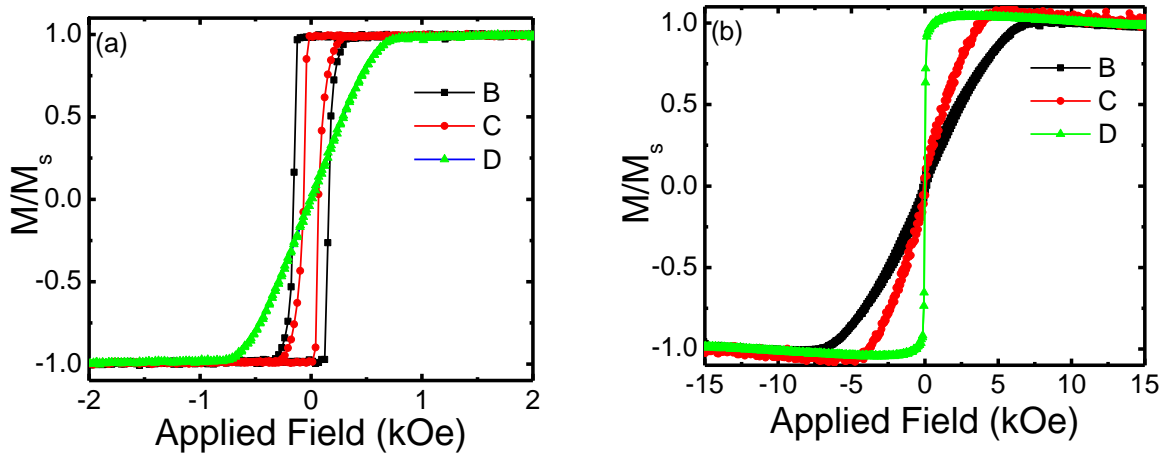


Figure 4.1. M-H loops of [Co/Ni]xN multilayers (a) out of plane (b) in-plane

We also performed frequency dependent measurements on the same sample series. Figure 4.2 (a) shows microwave frequency vs. resonance field data for 8ML sample. This data is fitted to the Kittel formula [50] $\omega = \gamma \sqrt{(H_{res} + H_k)(H_{res} + H_k + 4\pi M_{eff})}$ for out-of-plane anisotropy materials, and effective magnetization (M_{eff}) of the sample is evaluated. Figure 4.2

(b) shows line width vs. microwave frequency data which is fitted to the Gilbert damping formula $\Delta H_{pp} = \Delta H_0 + \frac{2\alpha}{\sqrt{3}\gamma} \omega$. The damping constant α is 0.02 for Co/Ni 8 ML's. For the series of samples with constant Co/Ni bilayer thickness, it was observed that, for the thickness range studied, as the number of multilayers increased, the damping constant decreased. This illustrates that, as the number of multilayers increases, the out of plane anisotropy increases, and hence the contribution from the demagnetizing fields which tend to keep the magnetization in the plane of the film decreases, and therefore the damping constant decreases.

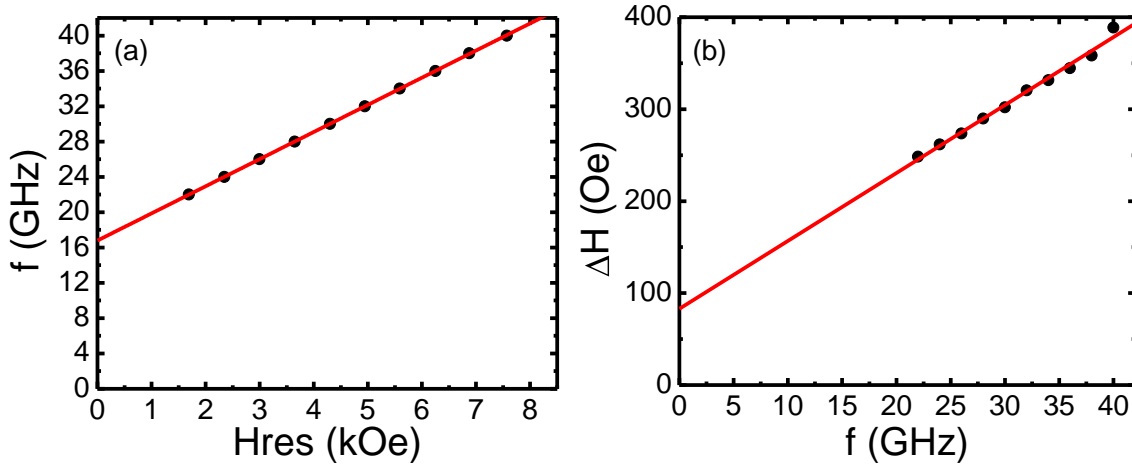


Figure 4.2: Microwave frequency measurements of [Co(0.3)/Ni(0.6)]x8 multilayered sample. (a) microwave frequency vs. resonance field. (b) linewidth Vs microwave frequency.

We have also deposited a series of samples of Co(0.3)/Ni(0.6)xN ML where N = 8,10 and 12 with a 0.5nm CoFeB on top of these multilayers. Figure 4.3 (a) and (b) shows out of plane and inplane loops respectively. It is clear from the out of plane loops that all the multilayers can pull 0.5nm of CoFeB out of plane. However, as the number of multilayers increases, the out of plane loops shows a bow tie shape. It is clear from the out of plane loops that as the number of multilayers increases from 8 to 10 and then to 12, the bow tie shape is increasing indicating the formation of stripe domains. However, there is no clear indication of saturation magnetic field in case of inplane loops. All the loops are saturating around 12 kOe.

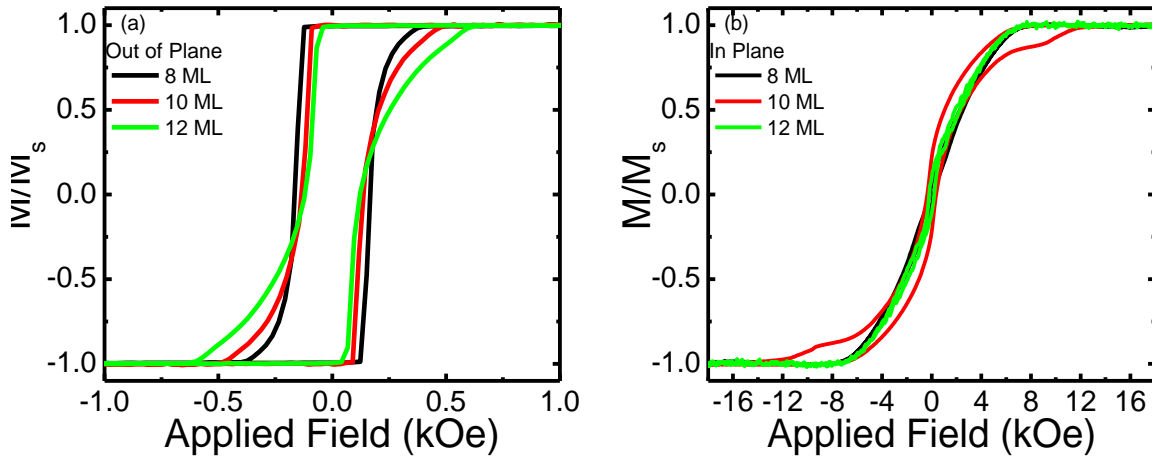


Figure 4.3. M-H loops of [Co/Ni] x N/CoFeB0.5 multilayers (a) out of plane (b) in-plane

Microwave frequency dependent measurements were done on a series of [Co(0.3)/Ni(0.6)] x N samples with and without a thin 0.5 nm thickness of CoFeB on top of the multilayers as shown in Fig 4.4 (a) & (b) respectively where N is the number of multilayers. As the number of multilayers increased from 6 to 12 keeping the Co/Ni thickness ratio constant, the damping constant and M_{eff} decreases indicating that the out of anisotropy increases with the increasing number of multilayers and hence the contribution from the demagnetizing fields which tends to keep the magnetization in the plane of the film decreases.

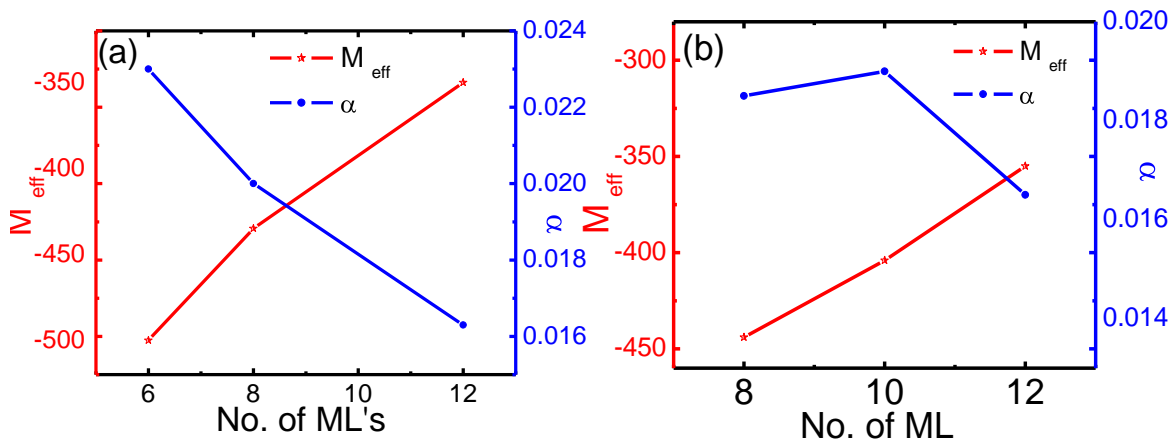


Figure 4.4. FMR measurements of [Co (0.3)/Ni (0.6)] x N multilayered samples (a) without CoFeB and (b) with CoFeB.

Figure 4.5 shows the anisotropy constant K_u values for multilayers with and without CoFeB. It was observed that, as the number of multilayers increased, the K_u values increased for both the series of samples indicating that the PMA increases with the number of multilayers for a constant bilayer thickness as observed in the magnetometry measurements. The corresponding saturation magnetization M_{eff} and damping parameter α values are listed in table 4.1

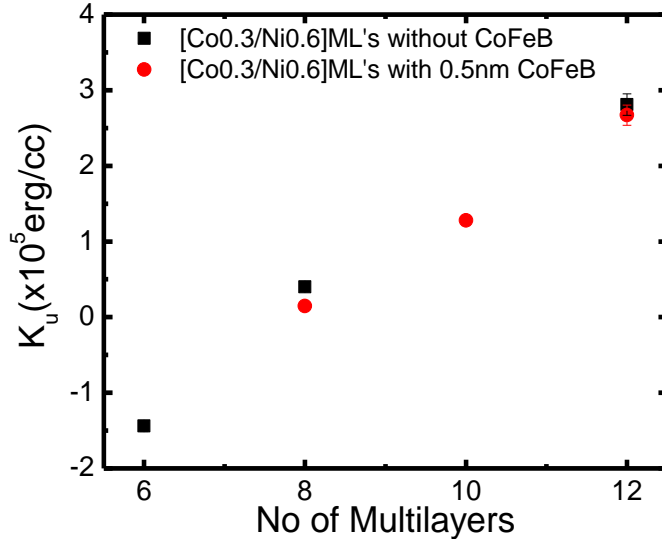


Figure 4.5: K_u Vs no of multilayers with and without CoFeB.

No of multilayers	M_s (emu/cm ³)	H_{eff} (kOe)	K_{eff} (ergs/cm ³)	K_u (erg/cm ³)	(α)
without CoFeB					
6	450	-6.2918	-1.42E+06	-1.44E+05	0.023
8	450	-5.473866	-1.23E+06	4.01E+04	0.02
12	450	-4.40426	-9.91E+05	2.81E+05	0.016
with CoFeB					
8	450	-5.587118	-1.26E+06	1.46E+04	0.019
10	450	-5.083774	-1.14E+06	1.28E+05	0.019
12	450	-4.467178	-1.01E+06	2.67E+05	0.017

Table 4.1: Summary of M_{eff} , K_u , and α values for Co/Ni multilayer series with and with of CoFeB.

Figure 4.6 shows the dependence of stress on number of Co/Ni multilayers. As the number of Co/Ni multilayers increases from 4 to 8, keeping the total thickness constant the films become more compressive as shown in 4.6 (a). However as the number of multilayers increases from 4 to 12 keeping the Co_{0.3}/Ni_{0.6} ratio constant, the films become less compressive as shown in figure 4.6 (b). However all the films showed compressive stress in as deposited samples.

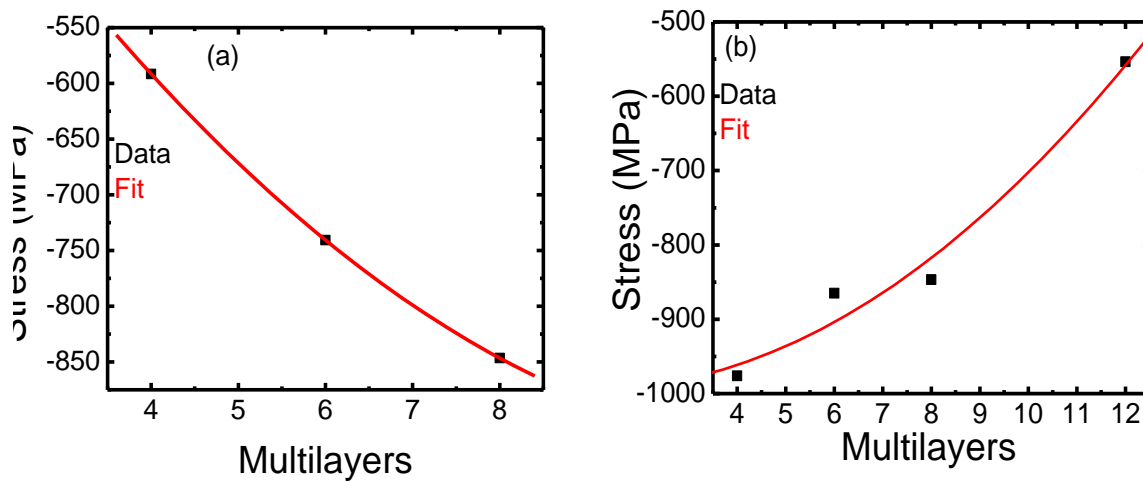


Figure 4.6. Stress vs number of multilayers (a) Total thickness of Co/Ni is kept constant (b) Co_{0.3}/Ni_{0.6} ratio is kept constant.

A laminated seed layer of Ta₅/Pt₁₀ nm was used to promote fcc (111) texture of the magnetic multilayers, as shown in figure 4.7 (a). A distinct fcc (111) peak at $2\theta \cong 43^\circ$ was observed indicating that the as-deposited ML's show the fcc structure of CoNi₂ initially proposed theoretically by Daalderop et al [49] and verified experimentally by Broesamle et al [47]. In order to study the extent of interdiffusion in these ML's we have carried out a local electrode atom probe (LEAP) analysis of the multilayers as shown in Figures 4.7 (b) and (c). Sphere mode LEAP analysis from figure 4.7 (b) clearly suggest that the Co and Ni multilayers are distinct without much interdiffusion.

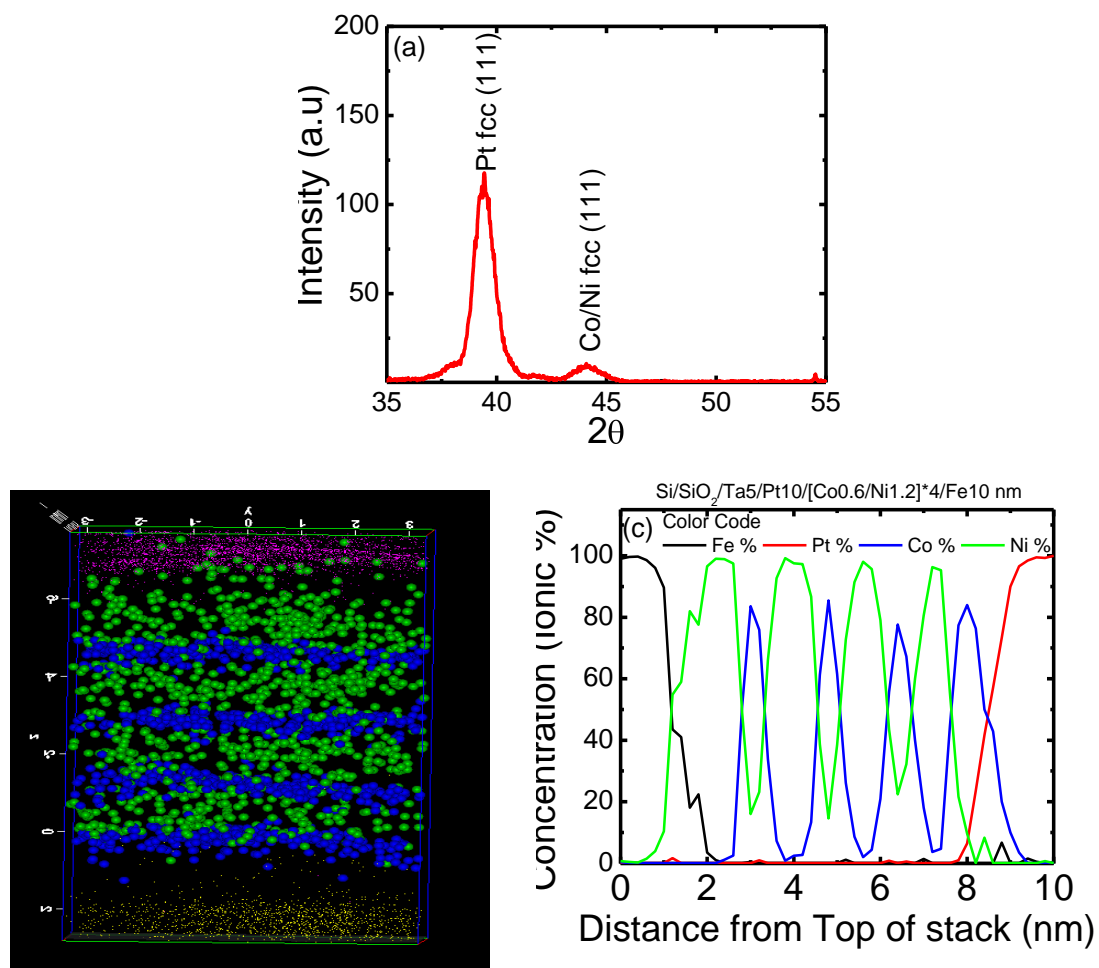


Figure 4.7: Structural characterization of $[\text{Co}(0.3)/\text{Ni}(0.6)]_x\text{N}$ multilayered samples. (a) XRD scan of Co/Ni Multilayer (b) LEAP image of sphere mode reconstruction of Co/Ni multilayers. (c) LEAP concentration profile of multilayers.

4.4 Conclusions

In conclusion, we have optimized the parameters such as bilayer thickness, bilayer ratio and number of bilayers to obtain perpendicular magnetic anisotropy (PMA) of Co/Ni magnetic multilayered stacks using different seed layers. The coercivity and out of plane anisotropy of these ML's have been optimized. Ferromagnetic resonance measurements were performed to obtain the M_{eff} and damping constant values. M_{eff} and damping constant values were obtained for these multilayered stacks with a thin CoFeB on top of it. As deposited stress measurements were

performed showing that the films become less compressive with increase in no of multilayers keeping the total thickness constant. Finally structural characterization was performed on these stacks showing that they have fcc (111) orientation with a very little interdiffusion. These multilayered combinations were used as free and pinned layers in magnetic tunnel junctions and excellent switching characteristics were seen, the details of which are shown in chapter 4.

V. Co/Pd Multilayers

5.1 Introduction

Although perpendicular magnetic anisotropy (PMA) was observed in Co/Ni multilayers by varying the bilayer thickness, bilayer ratio and number of bilayers, the seed layers below these multilayers play an important role in promoting the fcc (111) texture as well as PMA. In the previous chapter we have investigated Co/Ni PMA using different seed layers such as Ta/Pt and MgO. In order to realize a magnetic tunnel junction with perpendicularly magnetized free and pinned layers, Co/Ni multilayers grown on MgO barrier layer should be perpendicularly magnetized with respect to the film plane. However, PMA in Co/Ni multilayers was found to be strongly dependent on the seed layer. For instance, these multilayers showed in-plane anisotropy when grown on an MgO seed layer. In order to achieve PMA on top of the MgO barrier layer, different material systems have been studied by various researchers. Recent studies showed that Co/Pd multilayer structures have very high perpendicular magnetic anisotropy and easily tunable magnetic properties [51-54]. These multilayers were used in conjunction with conventional antiferromagnets such as FeMn, and IrMn [55-59] to study the perpendicular exchange coupling with antiferromagnets and also the exchange bias and tunnel magnetoresistance dependence on these structures. In-situ variation of growth properties such as layer thickness and sputter pressure are shown to be critical for tuning the magnetic properties of these Co/Pd multilayers such as coercivity and anisotropy constant K_u .

5.2 Results and discussion

We have investigated perpendicular magnetic anisotropy in Co/Pd multilayers. The magnetic anisotropy in Co/Pd ML's can be easily tailored by changing the thickness of the individual Co and Pd layers. We carried out a detailed study of these ML's, varying individual layer thicknesses, Co/Pd ratios and number of multilayers, before and after annealing. It was observed that Co/Pd ML's grown above MgO were lower in coercivity than those grown below MgO, with PMA observed for ML's grown above and below MgO. These Co/Pd multilayers can be used as pinned and free layers in pseudo MTJ's if they have a clear difference in coercivities. The thickness of the ferromagnetic Co layer was varied from 0.2 nm to 0.3 nm keeping the Pd thickness constant at 1 nm. These Co/Pd multilayers, when grown on Ta5/Pt10 nm seed layers showed very high coercivity for both four and nine multilayers; moreover the coercivity increased dramatically upon annealing these samples as shown in figure 5.1 (a). However, if MgO is used as a seed layer, the coercivity decreases for both as-deposited and annealed samples, as shown in figure 5.1 (b).

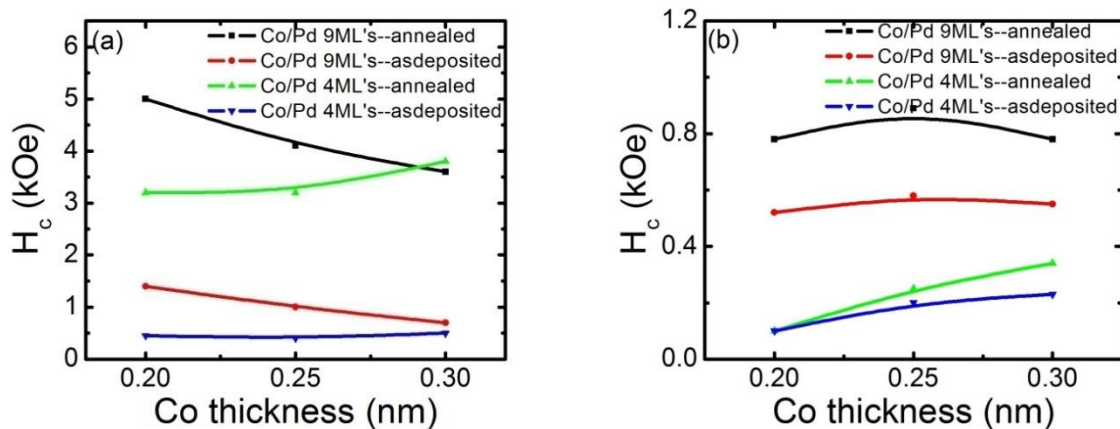


Figure 5.1: Coercivity vs. thickness of Co in Co/Pd multilayers for (a) Co/Pd as-deposited and annealed multilayers deposited below MgO barrier layer, and (b) Co/Pd as-deposited and annealed multilayers deposited above MgO barrier layer.

Perpendicular magnetic anisotropy is observed in all the Co/Pd multilayers below and above the MgO barrier layer. The remanent magnetization perpendicular to the film plane is almost identical to the saturation magnetization value indicating square loops. Our preliminary optimization study led to an MTJ design in which we deposited nine and four multilayers of Co/Pd below and above the MgO barrier layer for the reference and free layers, respectively.

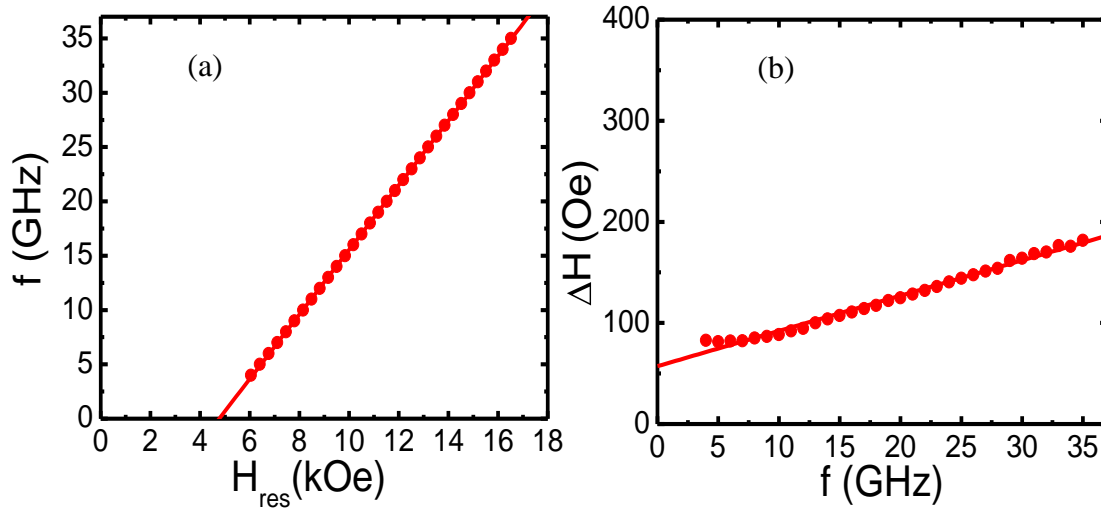


Figure 5.2: Frequency dependent FMR data of Co/Pd Multilayers with the field applied along the out-of-plane direction (a) frequency vs H_{res} (b) ΔH vs frequency.

We have performed frequency dependent FMR measurements on Co/Pd multilayers with CoFeB on top of these multilayers to investigate the amount of CoFeB that can be pulled out of the film plane. To quantify this, we determined the effective magnetization M_{eff} with $4\pi M_{eff} = 4\pi M_S - H_K$, by fitting the frequency data to the Kittel formula [50] with the fields ranging up to 17kOe applied along the out-of plane direction to ensure saturation as shown in Figure 5.2. Figure 5.3 (a) shows M_{eff} values for different thicknesses of CoFeB and it is clear that, as the thickness of the CoFeB on top of these multilayers increases, M_{eff} changes from negative to positive values, indicating a shift from PMA to in-plane behavior. Specifically, a 0.9 nm thickness of CoFeB is pulled out of plane by the Co/Pd ML's, but at higher thicknesses the

CoFeB goes in-plane. The negative M_{eff} indicates that the magnetization points out of the film plane. However, the observed resonance is most likely due to the CoFeB on top of these multilayers, which is also consistent with the strong dependence of M_{eff} on the thickness of CoFeB and the lack of an observable resonance for Co/Pd multilayers without CoFeB. The Gilbert damping parameter α is obtained by fitting the measured frequency dependence of the linewidth ΔH to the following formula [60]:

$$\Delta H = \Delta H_0 + \frac{2}{\sqrt{3}} \frac{\alpha}{\gamma} \omega \quad \dots\dots\dots (5)$$

The damping parameter α increases with decreasing CoFeB thickness as seen in figure 3 (b). One plausible origins for this is spin-pumping, which should scale with the inverse thickness of CoFeB [61].

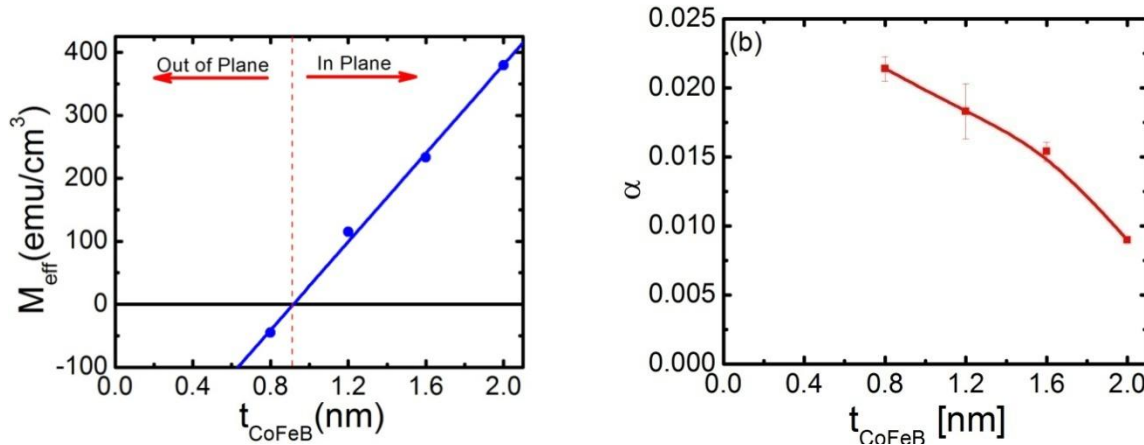


Figure 5.3: (a) M_{eff} vs thickness of CoFeB deposited on top of $[\text{Co}_{0.2}/\text{Pd}_1]_{*9}$ multilayers. (b) Damping constant vs thickness of CoFeB deposited on top of $[\text{Co}_{0.2}/\text{Pd}_1]_{*9}$ multilayers.

These PMA-based materials were deposited as full MTJ stacks with the structure: seed layer/ $[\text{Co}_{0.2}/\text{Pd}_1]_9/\text{CoFeB}_{0.4}/\text{MgO}_{1.6}/\text{CoFeB}_{0.4}/[\text{Co}_{0.3}/\text{Pd}_1]_4/\text{cap}$. These full MTJ stacks were characterized by magnetometry to ensure coercivity differences between the free and reference layers, as shown in Figure 5.4 for Co/Pd ML's under perpendicular applied fields. It can be seen

that the loop shows clear perpendicular anisotropy and the coercivities of the pinned layer and free layer are distinct.

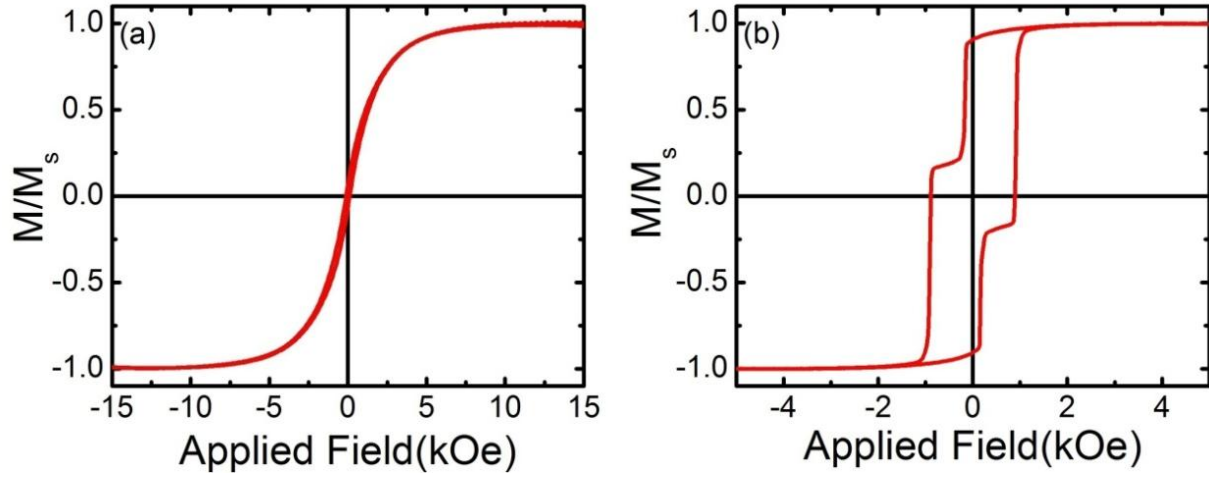


Figure 5.4: MH loops of pMTJ with Co/Pd ML's as free and reference layers (a) in plane loop and (b) out of plane loop. The MTJ stack is Pd (seed layer)/ (Co_{0.2}/Pd₁)₉/ CoFeB_{0.4}/ MgO_{1.6}/ CoFeB_{0.4}/(Co_{0.3}/Pd₁)₄/Ru (cap).

These stacks were then patterned into MTJ devices using a stepwise planarization technique developed by us at UA. This technique repeatedly uses a specific sequence of processing steps – pattern, etch, deposit, liftoff – in such a way that the device is kept planar at each critical phase of its fabrication. The critical aspect of this procedure is that the etch depth and the deposition thickness must match, so that the sample will be planar after the liftoff procedure. Figure 5.5 (a) and (b) shows field-switched transport characteristics at 100 K for the preliminary micron-sized devices fabricated using (a) Co/Pd ML's for free and reference layers, and (b) Co/Pd ML reference layer and Co/Ni bottom free layer. These samples are annealed at 300⁰C for 2 hours with an out-of-plane applied field of 5kOe. The field switching characteristics of the Co/Pd ML device is excellent. The seed used for the Co/Ni ML was Cu which is not as effective as Pt in promoting fcc (111) texture, and hence PMA, which explains why the free layer switching is not as sharp as the Co/Pd reference layer switching.

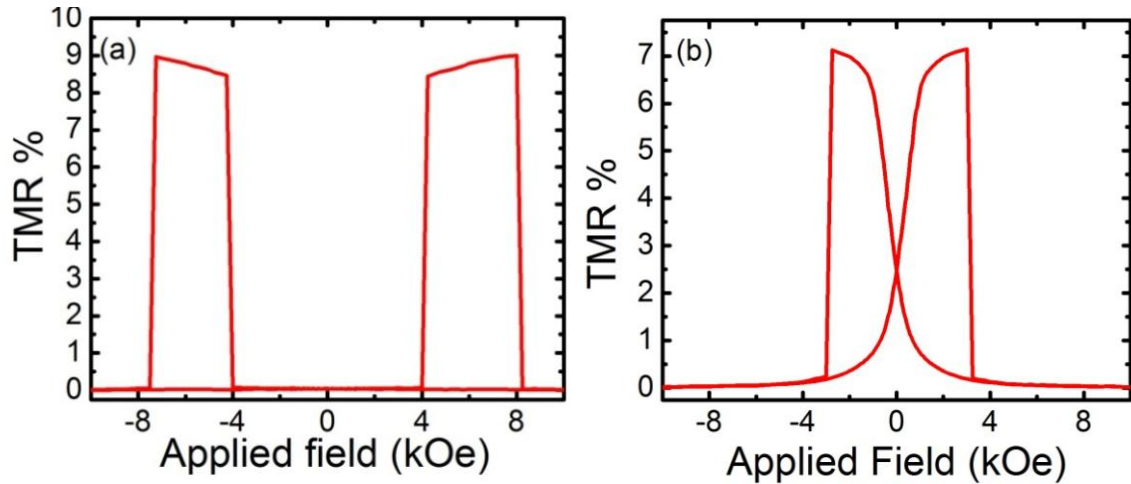


Figure 5.5: MR loops of (a) Co/Pd free and pinned layer and (b) Co/Pd pinned and Co/Ni free layer MTJ's at 100K.

Figure 5.6 shows the corresponding M-H loops of the above MTJ stacks measured on full film before patterning. It is observed that the MTJ with Co/Pd ML's as free and pinned layer with Pd seed layer has very clear difference in free and pinned layer switching as seen in figure 5.6 (a) corresponding to the R-H loop shown in figure 5.5 (a). However, the M-H loops of the MTJ stack with Co/Pd as pinned layer and Co/Ni as the free layer with a Cu seed layer does not show clear switching between the free and pinned layers as seen in figure 5.6 (b). The corresponding sloping behavior of the free layer in the R-H loop in figure 5.5 (b) is due the partial PMA of these Co/Ni ML's.

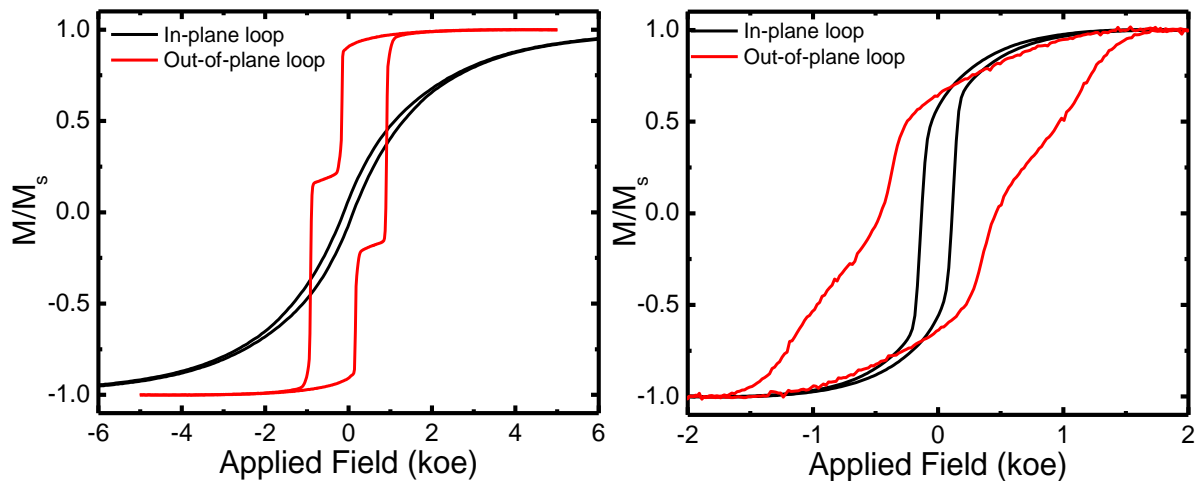


Figure 5.6: Out-of-plane MH loops of full MTJ stacks (a) Co/Pd free and pinned layer and (b) Co/Pd pinned and Co/Ni free layer MTJ's at 100K.

A comparison of Out-of-plane M-H loops of $[\text{Co}_{0.3}\text{Ni}_{0.6}]_4$ ML's with two different seed layers is shown in figure 5.7. The films show clear out of plane behavior with Ta/Pt seed layer indicating clear PMA. However, the same stack with Ta/Cu shows partial PMA.

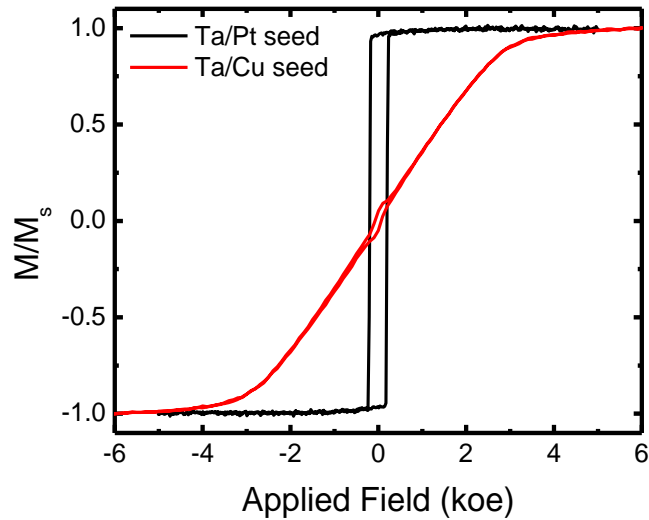


Figure 5.7: out-of-plane M-H loops of $[\text{Co}_{0.3}\text{Ni}_{0.6}]_4$ ML's with Ta/Pt and Ta/Cu seed layers.

5.3 Current Switching

Spin transfer switching measurements were performed on similar samples at our sponsoring company, Grandis, in August 2009. Both the free layer and pinned layer of the MTJ are Co/Pd ML's. The coercivities of the free and pinned layers are different, a so-called pseudo tunnel junction structure, allowing both parallel and antiparallel alignment of free and pinned layers under the applied magnetic fields. The coercivities of the pinned layer and the free layer in the continuous film were 200 Oe and 500 Oe respectively. However, the coercivities increased dramatically once the film was patterned into nano devices. The coercivity of the free layer increased from 200 Oe to 1800 Oe after patterning. Similar enhancements in coercivity were

observed earlier [62]. This enhancement is because of the different mechanisms involved in switching of the continuous layer as opposed that of the nano-patterned devices. In a continuous full film, the reversal occurs mainly because of domain wall nucleation and growth, and coherent switching is the dominant mechanism in patterned devices. Although the optimized free layer coercivity of the full film multilayers was low, the coercivity increased dramatically after patterning. In order to observe current switching in these samples, application of a bias field (H_b) was required during measurement. Due to this, we could not estimate the actual current required to switch the free layer and also the thermal stability factor, Δ (ratio of $K_u V/k_B T$) value for these devices. Initially a very large field was applied on these devices to saturate both the free layer and pinned layer in one direction and establish an initial state of the device, then a bias field, H_b , less than the coercive field of the free layer, H_c , was applied in the direction opposite to the initial applied field. In our case, the applied bias field is 1650 Oe and the coercive field is 2000 Oe. After determining the current direction for switching, the current is increased from zero until the free layer is switched; subsequently, the current is reversed to switch back the free layer as shown in figure 5.8.

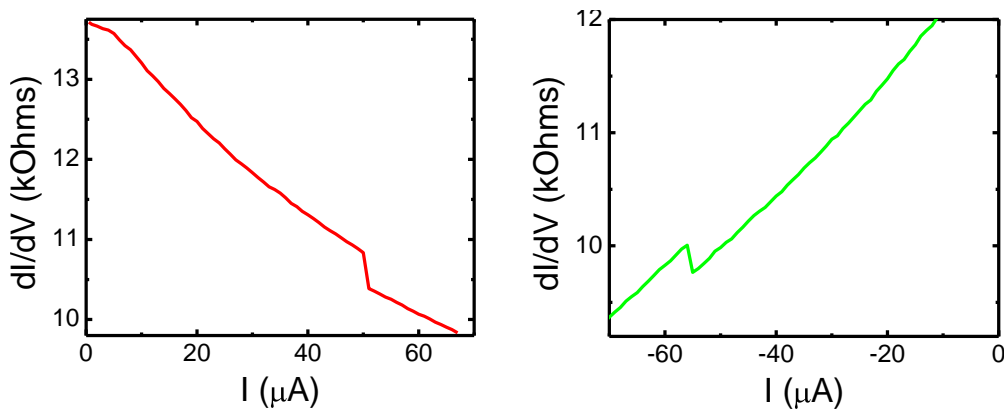


Figure 5.8: dI/dV versus I for bias field H_b of 1650 Oe, showing transitions from parallel to antiparallel states of free layer.

TMR of about 7.8% percent was observed on these current switched samples, in good agreement with the field switching TMR data. However, the current required for switching devices is too high, probably because of the high thermal stability of these devices, and hence field bias was required in this case.

5.4 Inelastic tunneling spectroscopy (IETS)

We have also performed inelastic electron tunneling spectroscopy (IETS) on these MTJ's to measure the characteristic phonon and electronic spectra obtained from the MgO barrier layer that is an indicator of the quality of the MgO and compare this with the calculated MgO phonon densities of states, electron energy loss spectra, and inelastic neutron scattering data. The data presented here is done on the sample whose transport characteristics are shown in figure 5.5 (a), a MTJ with Co/Pd free and pinned layers.

Inelastic electron tunneling spectroscopy (IETS) is a spectroscopy technique that has been extensively used to measure the characteristic spectra of a specimen. By measuring currents and voltages across a MTJ device, one is able to extract the spectroscopic information about the MgO barrier layer in the MTJ device. An important advantage of IETS is its ultra-high sensitivity, i.e less than 10^{13} molecules are required to provide a spectrum; and also, it is easier to identify fundamental properties such as overtones and combination bands, which are exceptionally weak and difficult to identify by other techniques such as IR or Raman spectroscopy.

The IETS measurement setup is similar to the normal four point setup where in the two probes are used to introduce the current across the junction and the other two probes are used to measure the potential difference across the specimen. When a voltage is applied the electrons can tunnel from one ferromagnetic layer to the other by two different pathways. It can either

elastically tunnel through the barrier to reach the Fermi level of the other electrode by emitting a photon or exciting a phonon. In the other path the electron can tunnel through the barrier by losing energy while tunneling through the barrier by exciting a phonon or vibration mode of a molecule in the barrier material. The latter is referred to as inelastic tunneling as shown in figure 5.9.

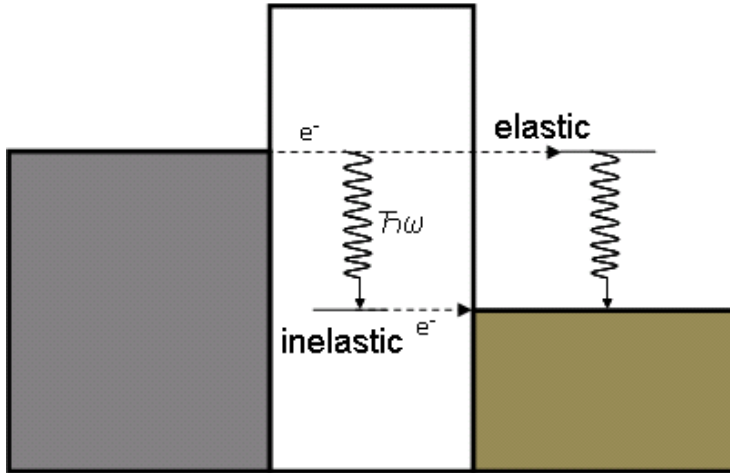


Figure 5.9: Inelastic and elastic tunneling pathways.

The total tunneling current through the junction is the sum of both inelastic and elastic pathways; however, the contribution from inelastic tunneling is in general relatively small as compared to elastic tunneling and only occurs when the applied voltage is high enough such that an electron is able to excite a phonon or vibration mode. This is visible in the I-V curve as a slight increase of the slope as shown in the figure 5.10.

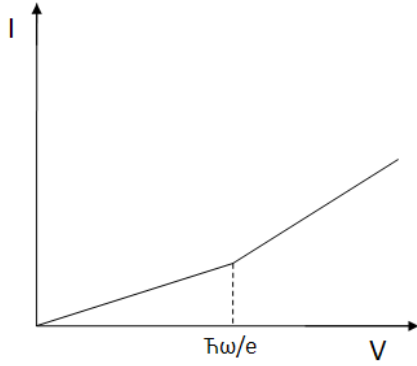


Figure 5.10: A typical I-V plot as a result of IETS. A slight increase in slope is observed when the voltage is high enough indicating the inelastic tunneling.

Since it is difficult to determine the exact voltage at which the slope increases, the first and second derivatives of current vs voltage are examined and the respective typical plots for these are shown in figure 5.11.

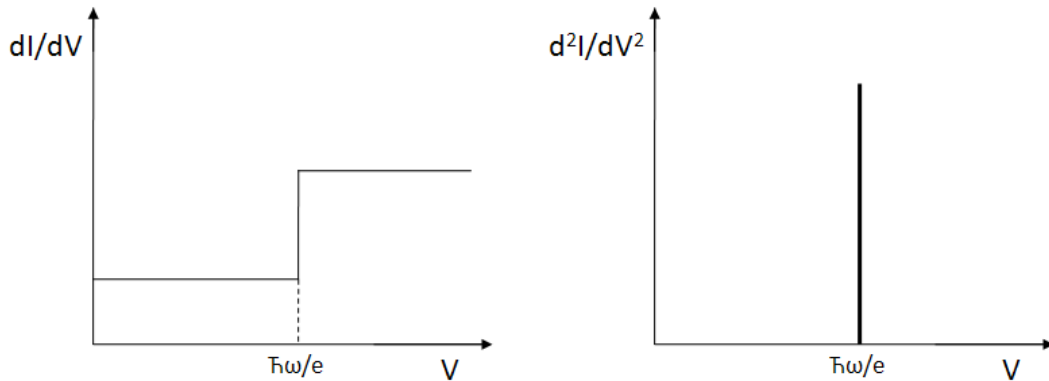


Figure 5.11: First and second derivatives of I wrt to V. 2nd derivative plot clearly shows the slight change in the slope as a peak.

The details of the experimental setup used to measure this second derivative signal are explained in chapter 3. Inelastic tunneling spectra (d^2I/dV^2 vs V) were taken at $T = 2.0\text{K}$ with an ac modulation of 5mV in a field of $\mu_0 H_{\text{ext}} = 0.7\text{T}$ (i.e., the antiparallel magnetization state) on the sample shown in figure 5.5(a). A polynomial background was subtracted, obtained by fitting the high and low bias data well away from the peak-containing region of the spectra. The resulting

‘background-corrected’ spectra were then compared with measured and calculated MgO phonon densities of states, electron energy loss spectra, and inelastic neutron scattering data is shown in figure 5.12. MgO has six phonon branches: one longitudinal acoustic, one longitudinal optical, two transverse optical, and two transverse acoustic. Transverse optical phonon frequencies for MgO are reported at $\omega_{TO} \approx 49\text{-}55$ meV. Transverse acoustic modes are reported at $\omega_{TA} \approx 35\text{-}37$ meV. Longitudinal acoustic and optical frequencies are $\omega_{LA} \approx 48\text{-}52$ meV and $\omega_{LO} \approx 69, 89$ meV.

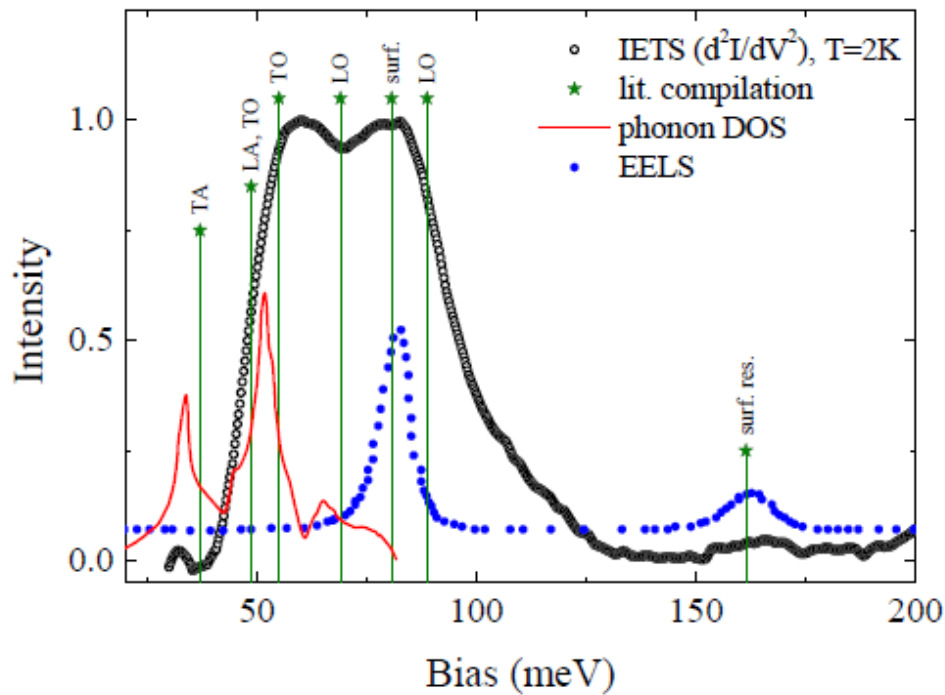


Figure 5.12: Background-corrected IETS spectra compared with compiled literature data, EELS, and a phonon DOS calculation.

The known optical modes observed in this sample agree roughly with the observed IETS spectra, as is typically the case for Al₂O₃-based junctions, though possibly somewhat higher in energy than reported values. This may be because of the strain between the ferromagnetic electrode and MgO barrier layer in the sample, the peaks shift by about 5 to 10 meV. The

acoustic modes are not clearly observed. However, they occur at relatively low energies, where the background spectrum is dominated by magnetic excitations, and they may simply be obscured. However, the gross features of the spectra are adequately reproduced by considering the bulk and surface vibrational modes of MgO.

5.5 Conclusions

In conclusion, we have optimized various types of perpendicular magnetic anisotropy (PMA) magnetic multilayered stacks using different seed layers. The coercivity and out of plane anisotropy of these ML's have been optimized. Ferromagnetic resonance measurements were performed to obtain the M_{eff} and damping constant values. These multilayered combinations were used as free and pinned layers in magnetic tunnel junctions and excellent switching characteristics were seen. We have performed both the field and current switching measurements on these devices. The TMR values obtained in case of field switching are about 10% at 100K which is very low as compared to conventional MgO-based in-plane MTJ's reported in the literature. We believe the fundamental problem in not obtaining TMR values greater than 10% is caused by the lattice mismatch between the fcc (111) PMA-ML's and MgO/CoFeB bcc (001) layers, combined with the necessarily thin (~0.5 nm) layers of CoFeB used in these junctions to maintain perpendicular anisotropy. The TMR values obtained with current switching is about 7.8 % on similar samples, however, the currents required to switch between parallel and antiparallel states of free and pinned layer was too high, so a bias field was applied during these measurements to assist current switching. We have also performed IETS measurements on these tunnel junctions to probe the MgO barrier layer quality and also to measure the characteristic spectra of the MgO barrier layer by comparing with the calculated MgO phonon densities of states, electron energy loss spectra, and inelastic neutron scattering data.

VI. Crystalline Alloys

6.1 Introduction

In previous chapters we have investigated the perpendicular magnetic anisotropy (PMA) of Co- based multilayered stacks, which were used as pinned and free layers for CoFeB/MgO/CoFeB-based magnetic tunnel junctions. Although these multilayered pinned and free layers have perpendicular magnetic anisotropy, which will reduce the critical current density for switching as theoretically predicted, the tunnel magnetoresistance of these MTJ's was very low compared with conventional in-plane anisotropy materials, never exceeding 10%, independent of where and how the device fabrication was carried out. The low TMR is believed to be caused by the lattice mismatch of the pinned and free layers with the FM/MgO/FM trilayer thought to be responsible for the giant TMR through the symmetry spin filtering effect [22]. These Co-based multilayered stacks have fcc (111) orientation, and hence we hypothesize that the transition from each fcc (111) perpendicular multilayered stack to the MgO-templated bcc (001) CoFeB ferromagnetic layers on either side of the MgO barrier inhibited the symmetry filtering effect and resulted in low TMR [63]. Although these multilayered perpendicular magnetic anisotropy (PMA) materials can satisfy two important criteria: 1) low switching current and 2) high thermal stability for pMTJ's, it is observed that these stacks have low tunnel magnetoresistance for the reasons described above [58, 64 & 65].

We have investigated the PMA of $L1_0$ ordered alloys which can be used in pMTJ's. These alloys are good candidates for pMTJ's because they have large perpendicular magnetic anisotropy due to their high K_u values of the order of 10^7 erg/cm³ with a (001) easy axis. This

high K_u value is very important for obtaining good thermal stability for nanometer sized elements. Moreover, they have a very small lattice mismatch with the (001) CoFeB or MgO barrier, which may be critical for achieving high TMR values. However, these $L1_0$ materials are very sensitive to parameters such as the orientation of the substrate and the buffer or the seed layer and also on the temperature during deposition [66]. It is also important to achieve the $L1_0$ phase in these alloys at moderate temperatures for compatibility with CMOS processing for STT-RAM. Several researchers have already successfully grown these $L1_0$ alloys such as FePt, CoPt with (001) which can be used as magnetic media because of their high magnetic anisotropy values. MTJs with a $L1_0$ -ordered FePt alloy electrode as the pinned layer and FeCo as the soft free layer were fabricated by using an Al_2O_3 barrier layer prepared by a multiple oxidation process by researchers at Tohoku University [36]. They observed TMR of 18% and 40% at RT and 4.2 K, respectively. In another experiment, researchers at Toshiba Corporation [37] obtained over 100% TMR by using $L1_0$ -ordered FePt alloy electrodes as both free and pinned layers; however, different annealing conditions were required to obtain the coercivity difference in both the top and bottom electrodes. The key for the large TMR was the insertion of 3nm of Fe on either side of the barrier layer, which reduces the lattice match between the barrier and electrodes. A very low TMR of 6% was obtained if CoPt electrodes [38] are used for the free and pinned layers because of the large lattice mismatch between the electrodes and the barrier layer.

We attempted $L1_0$ growth of $Fe_{50}Pd_{50}$, $Fe_{50}Pt_{50}$, $Co_{50}Pt_{50}$, and $Co_{50}Pd_{50}$. We tried various substrates, for instance, MgO (001) single crystal substrates pretreated to remove contaminants, a variety of seed layers, various deposition techniques such as the so-called “layer-by-layer growth” [67], and various annealing techniques, both in-situ and ex-situ. However, except for the CoPd alloy, we could not achieve perpendicular magnetic anisotropy in any of these alloys.

We have studied the effect of different seed layers, deposition temperature and the thickness of the CoPd alloy on the PMA and the $L1_0$ phase of the $Co_{50}Pd_{50}$ alloy. $Co_{50}Pd_{50}$ alloy was deposited by co-sputtering pure Co and Pd targets. The deposition rates of Co and Pd were adjusted so as to achieve the desired atomic ratio of Co:Pd for the alloy, with deposition powers ranging from 140 to 300W. A range of materials, for instance, MgO or Ta/Pt or Ta/Pd were used as seed layers to promote PMA, as well as $L1_0$ growth. In-situ lamp annealing was utilized, both before and after CoPd alloy deposition to study the effect of deposition temperature and post-deposition annealing on the crystal structure and PMA properties. The magnetic and structural properties of the as-deposited and annealed samples were characterized by alternating gradient magnetometry, ferromagnetic resonance and X-ray diffraction.

6.2 Thickness dependence of PMA in $Co_{50}Pd_{50}$ alloys

A series of samples with varying thicknesses of $Co_{50}Pd_{50}$ alloy were deposited on Si (100) substrates with a buffer/seed layer of 10 nm of sputter-deposited MgO layer. A 450 °C in-situ lamp anneal was performed immediately after the deposition of the CoPd alloy. The sample structure was: Si(100)/MgO10/ $Co_{50}Pd_{50}$ (x)/anneal (450 °C)/MgO3nm, where (x) = 10, 20, 35, 50, 75 and 100 nm. Figure 6.1 (a) and (b) shows both the in-plane and out-of-plane M-H loops for these samples, indicating an increase in PMA with thickness. At 10 nm CoPd thickness, the sample shows in-plane behavior (not shown in Figure 1).

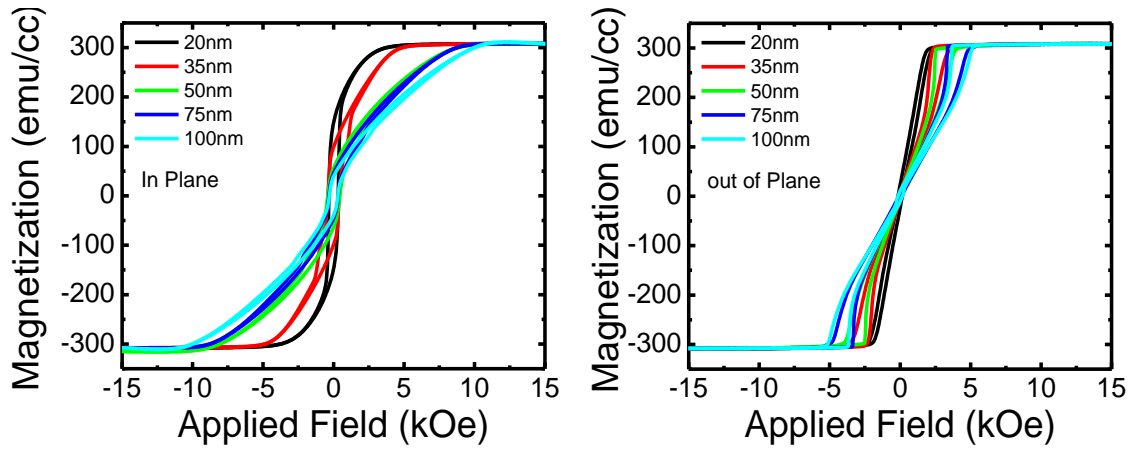


Figure 6.1. (a) In-plane and (b) out-of-plane M-H loops of $\text{Co}_{50}\text{Pd}_{50}$ alloys as a function of thickness, showing increasing perpendicular magnetic anisotropy with thickness.

All the samples showed a very low saturation magnetization of about 320 emu/cc. As the thickness of the $\text{Co}_{50}\text{Pd}_{50}$ alloy increases the PMA also increased. This can be observed by the increase of H_{eff} field in the inplane loop as the thickness increases. Also, as the thickness increases the nucleation field increased as seen in out of plane loops with a clear bow-tie shape in the thicker films, indicative of multi-domain behavior typically termed “stripe domains”. This may be because of strong intergranular exchange coupling between the magnetic grains which is typical of many perpendicular anisotropy continuous magnetic films. It is expected that, after these continuous films are patterned into nanosized devices, this multi-domain behavior will disappear. The nucleation field should change from negative to positive due to the decrease in demagnetizing field and also the remanent magnetization should increase, resulting in squarer loops.

Figure 6.2 shows the anisotropy constant K_u values for the thickness series investigated. It was observed that, as the thickness increased, the K_u values increased and the squareness decreased, indicating that the thicker films exhibited more pronounced multi-domain behavior.

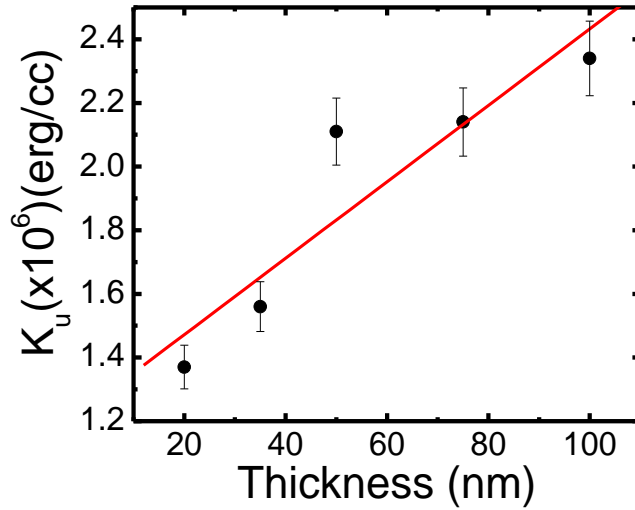


Figure 6.2: K_u vs. thickness of $\text{Co}_{50}\text{Pd}_{50}$ alloy.

The saturation magnetization, H_{eff} , K_{eff} and K_u values of these samples are listed in Table 1.

Thickness (nm)	M_s (emu/c m^3)	H_{eff} (kOe)	K_{eff} (ergs/ cm^3)	K_u (erg/ cm^3)
20	307	5.1	7.83E+05	1.37E+06
35	307	6.3	9.67E+05	1.56E+06
50	307	9.9	1.52E+06	2.11E+06
75	307	10.1	1.55E+06	2.14E+06
100	307	11.4	1.75E+06	2.34E+06

Table 6.1: Summary of magnetic properties of $\text{Co}_{50}\text{Pd}_{50}$ samples as a function of thickness.

X-ray diffraction has been carried out on these samples to investigate the crystal structure of the $\text{Co}_{50}\text{Pd}_{50}$ alloy. Although these films showed out of plane anisotropy, an fcc (111) orientation was observed in these films for all the seed layers attempted. Figure 6.3 below shows the fcc (111) phase present in the $\text{Co}_{50}\text{Pd}_{50}$ alloy for Ta/Pd, Ta/Pt and MgO seed layers respectively. There was no sign of an (001) L_{10} phase in any of the spectra. There are relatively few papers on $\text{Co}_{50}\text{Pd}_{50}$ alloys, and none of them report L_{10} phase formation. One paper reports a fairly low temperature transition from hcp to fcc at about 200 $^{\circ}\text{C}$ [68-69].

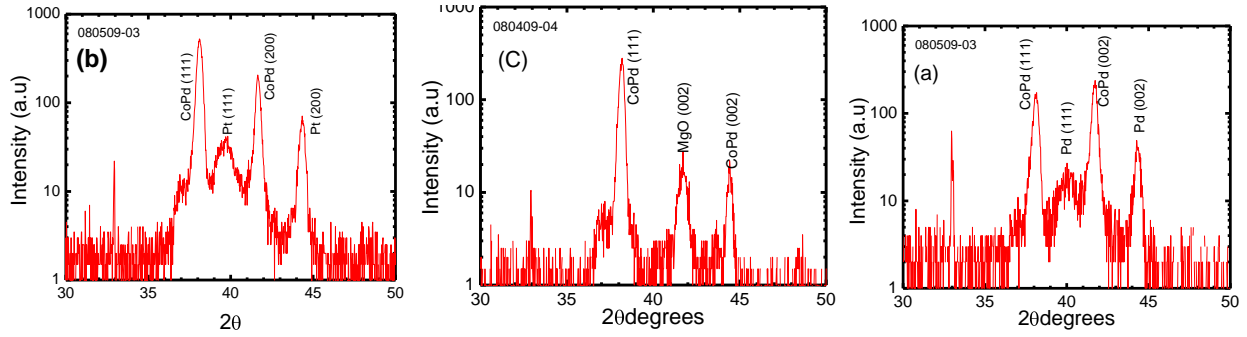


Figure 6.3: XRD pattern of $\text{Co}_{50}\text{Pd}_{50}$ alloy showing fcc (111) orientation with (a) Ta/Pd, (b) Ta/Pt and MgO seed layers respectively.

6.3 Temperature dependence of PMA in CoPd alloys

It is observed that there is a specific range of (pre- or post-) deposition temperatures in which the $\text{Co}_{50}\text{Pd}_{50}$ films are out-of-plane. This range of temperatures is from approximately 400 $^{\circ}\text{C}$ to about 500 $^{\circ}\text{C}$. A deposition temperature of around 550 $^{\circ}\text{C}$ yields in-plane magnetization in the

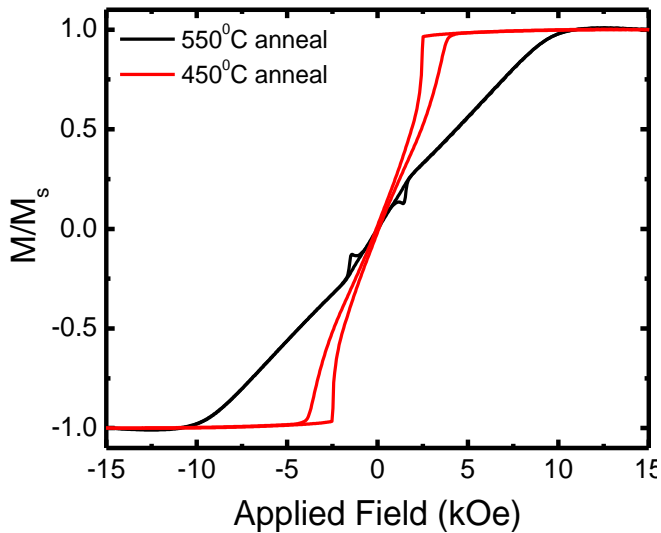


Figure 6.4: Out of plane loops of 35nm $\text{Co}_{50}\text{Pd}_{50}$ alloy films at at 550 $^{\circ}\text{C}$ and 450 $^{\circ}\text{C}$ temperature respectively.

films and moderate deposition temperature of 450 $^{\circ}\text{C}$ yields out of plane magnetization in the $\text{Co}_{50}\text{Pd}_{50}$ 35nm film as shown in Figures 6.4.

6.4 Seed layer dependence of PMA of CoPd alloy

Three different types of seed layers are used to grow CoPd alloy on top of Si (100) substrates. The seed layers used are Ta/Pd, Ta/Pt and MgO. It is observed that PMA is achieved on all the 3 types of seed layers indicating that the seed layer is not as critical for achieving PMA for this alloy as for some others, especially $L1_0$ materials. Figure 6.5 (a), (b) and (c) show the out of plane loops for a 35 nm thick $Co_{50}Pd_{50}$ alloy, with Ta/Pd, Ta/Pt & MgO seed layers respectively. All the loops look similar, with the bow-tie shape typical of multi-domain structures (stripe domains). This is similar to behavior shown by hcp $Co_{80}Pt_{20}$ alloys.

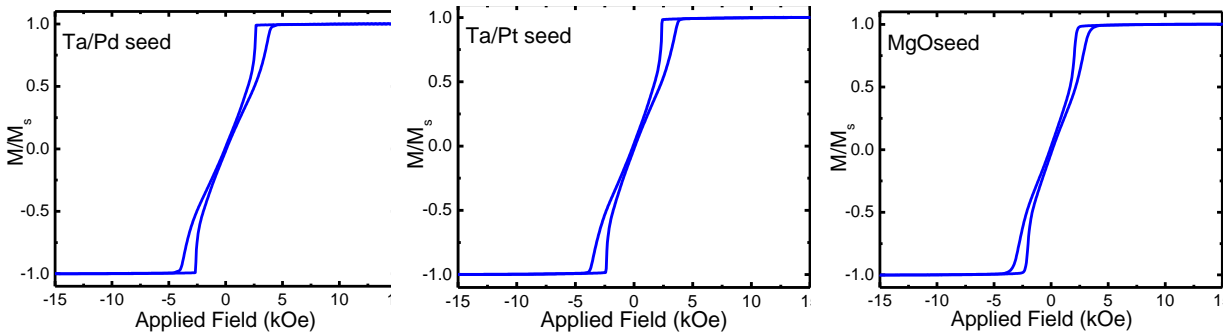


Figure 6.5: out of plane loops of $Co_{50}Pd_{50}$ 35nm alloy, with (a) Ta/Pd, (b) Ta/Pt & (c) MgO seed layers respectively.

6.5 Conclusions

In conclusion, we have deposited CoPd alloy films and observed perpendicular magnetic anisotropy in films greater than 20 nm thick, deposited between 400 and 500 °C. As the thickness of the CoPd alloy increased from 20 to 100nm, the PMA increased in these alloy films. This is indicated by the plot of K_u vs thickness. Also, as the thickness increased the films showed increasingly slanted bow-tie shaped out of plane loops indicating multi-domain structures. It is also observed that the PMA of these alloys seems to be dependent on the annealing temperature: the films go from out-of-plane configuration to in-plane configuration as the annealing temperature increases from 450C to 550C. Finally, it is observed that the PMA of the films is

independent of the seed layer used; clearly indicating that out of plane anisotropy in these films is not because of the growth from the seed layer. XRD analysis shows that the films grow with fcc (111) orientation and there is not (002) in these films indicating that the films doesn't have any $L1_0$ phase.

VII. Rare Earth Transition Metal (RE-TM) Alloys

7.1 Introduction

Amorphous rare earth transition metal alloys (RE-TM) were extensively studied for magneto-optic applications such as high density magnetic storage data. One of the best candidates for this type of storage media was amorphous TbFeCo films. These films have perpendicular uniaxial magnetic anisotropy which makes them thermally stable. Also the Curie temperatures of these materials are in the range of 400 to 600K which makes them suitable to write by heating with a laser. Other advantages include tunable magnetization and coercivity and low media noise which make them good candidate for media applications.

Recently, the RE-TM alloys [33-35] were studied for spintronic applications because of some of the reasons listed above. As discussed previously in chapters 4 and 5, perpendicular magnetic anisotropy materials are suitable for STT-RAM applications because of their good thermal stability and lower aspect ratios. RE-TM alloys are being studied for STT-RAM applications because of their PMA and tunable magnetic properties such as saturation magnetization, coercivity and Curie temperatures, which can be tailored to meet the requirements. Recently, there have been some reports on the use of RE-TM materials as electrode layers in pMTJs. Ohmori *et al.* [35] used 100 nm thick RE-TM free (GdFeCo) and pinned layers (TbFeCo) with 3nm of Fe layers on either side of the MgO barrier layer. They showed that the MgO barrier layer can be crystallized to (001) texture at lower annealing temperatures using the above structure. Higher temperature annealing may destroy magnetic properties of RE-TM alloys, moreover the thicker free and pinned layers may contribute to

higher RA values. On the other hand, Nakayama *et al.* [34] used different thickness of TbFeCo as free and pinned layers to achieve different coercivities for switching at different fields. Although, with a very thin free layer, they could successfully demonstrate spin transfer switching, the coercivity of free layer was still very high at 1.2 kOe, which may not be useful for practical STT-RAM applications. Hence it is a challenge to fabricate an ultrathin RE-TM film with low free layer coercivities and good PMA just by varying the composition of the alloy film. One another way to modify the magnetic properties in addition to the variation in composition was to modify the seed and cap layers for these RE-TM alloys. Several different combinations of under and overlayers were used by other researchers such as W [70], Al [71-73], Ag [74], TiN [75], AlN [76], which can provide both oxidation protection and coercivity enhancement. In this chapter we have studied the effect of thickness of TbFeCo on its PMA. The effect of temperature, seed and cap layers on PMA and coercivity are discussed.

7.2 Experimental details

The TbFeCo alloy was deposited by co-sputtering from individual Tb, Fe and Co targets, using dc magnetron sputtering. The rates of Tb, Fe and Co were adjusted such that Tb₂₁Fe₇₂Co₇ at% alloy films were obtained by co-sputtering. Deposition powers ranged from 50 to 450 W and the deposition pressures were held at 2 mTorr. M-H loops were measured using alternating gradient magnetometry.

7.3 Thickness dependence on PMA of TbFeCo

We have deposited a series of thick samples of TbFeCo on Si/SiO₂ (001) wafers. The structure of the films is Si/SiO₂/TbFeCo(x) where (x) = 12, 24, 36 and 48. None of the samples had any cap layers. It was observed that 12 and 24 nm films showed in-plane anisotropy. Figure 7.1 shows the in-plane and out of plane M-H loop, and it is clear that the loop has an in plane

easy axis with very low coercivity and high remanent magnetization. Figure 1 shows the out-of-plane loop; the saturation magnetic field of this loop is 8 kOe and very low remanent magnetization, indicating that the loop has an out-of-plane hard axis. The structure of the films is

Si/SiO₂/TbFeCo (X)

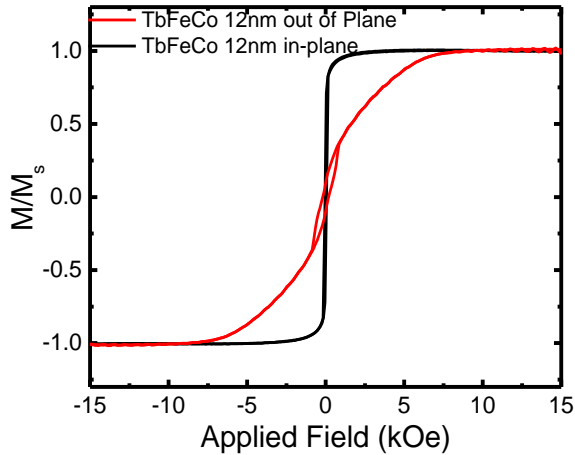


Figure 7.1: In-plane and out-of-plane M-H loops of 12nm TbFeCo film.

Upon increasing the thickness of the TbFeCo films, the loops show a transition from in-plane anisotropy to perpendicular anisotropy. Figure 7.2 shows the in-plane and out-of-plane loops of 36nm TbFeCo films, indicating that the films have perpendicular anisotropy, which is seen up to 150 nm thickness (thickest films deposited).

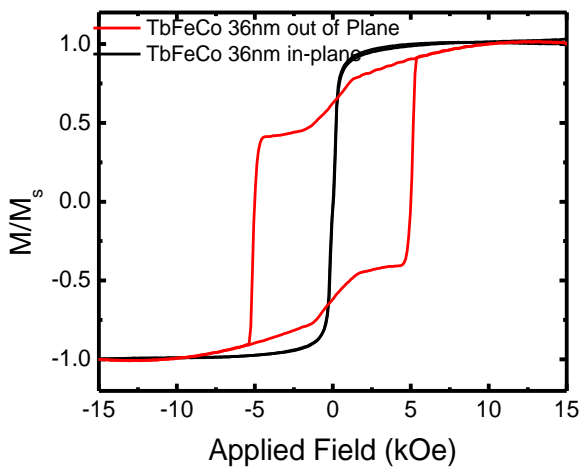


Figure 7.2: In-plane and out-of-plane M-H loops of 36nm TbFeCo film.

A possible reason for this transition might be the oxidation of the Tb for thinner layers [77-78], thereby effectively taking it out of the alloy magnetically. The thickness series samples were deposited on SiO₂ wafers without a cap layer. It is known that Tb is very reactive to oxygen and hence the thinner layers may be behaving like FeCo, which usually has in-plane anisotropy.

7.4 Thickness of CoFeB on TbFeCo

We have deposited a series of samples of samples with increasing thickness of CoFeB on top of TbFeCo to determine the amount of CoFeB that can pulled out of plane due to the magnetic exchange coupling between TbFeCo and CoFeB layers. It is interesting to observe that about 48nm TbFeCo can pull 2nm of CoFeB out of plane. Similar results were observed from researchers at Toshiba [2] where they have used 1 nm of CoFeB on either side of MgO, coupled with thicker TbFeCo layers. Figure 7.3 (a) and (b) show both the in- plane and out-of-plane loops of increasing thickness of CoFeB on top of TbFeCo layer. As the thickness of the CoFeB layer increased, the saturation magnetization field for in-plane M-H loops decreased, indicating that 2nm CoFeB samples were weakly coupled, compared with 0.4nm CoFeB samples. Figure 7.3(b) shows the out of plane M-H loops: all the loops look similar, with a coercivity of about 5kOe. However, there was a small kink at near zero fields for all the samples. This type of kink was observed by other researchers also. One possible reason for this kink at near zero fields is the oxidation of the TbFeCo film at the interface.

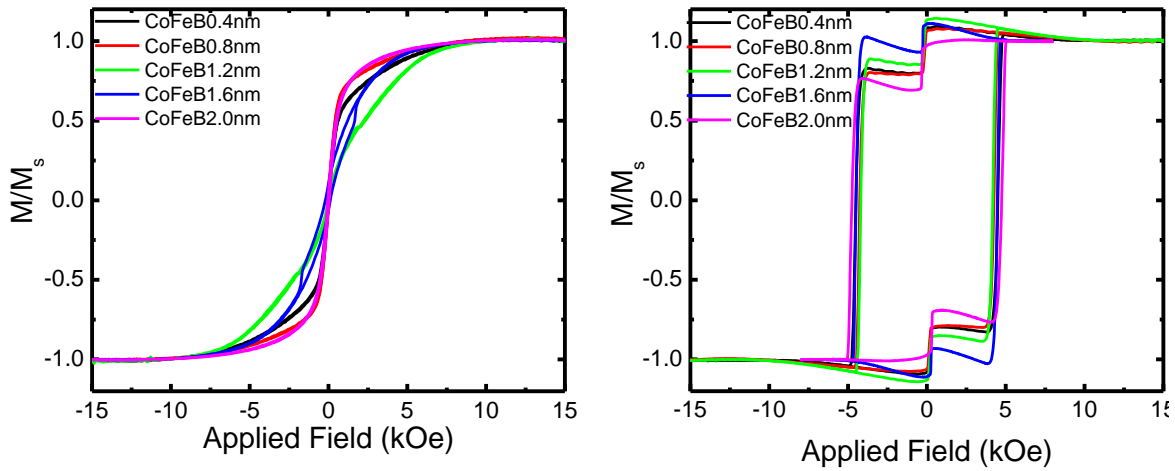


Figure 7.3: M-H loops of increasing thickness of CoFeB on top of TbFeCo (a) in-plane (b) out-of-plane loops.

7.5 Seed layer and annealing dependence on PMA and Coercivity of TbFeCo

Since TbFeCo is extremely susceptible to oxidation, search for a good buffer material that prevents oxidation of the Tb and enhances the magnetic properties is very important. We have investigated the effect of different seed layers grown on different substrates on the PMA and coercivity of TbFeCo. Although the primary purpose of the seed layers and the cap layers were to protect TbFeCo from oxidation, it is interesting to observe that the coercivity of the TbFeCo varies dramatically with the underlayers. As seen in figure 7.4, the coercivity increased from 10kOe to 15kOe for TbFeCo films on MgO seed layers deposited on SiO_2 substrates, as compared with films on single-crystal (001) MgO substrates. Although the mechanism involved in this dramatic increase of coercivity with different seed layers is not completely understood, one of the plausible explanations would be pinning sites which impede domain wall motion in the TbFeCo film. The increase in coercivity may be because of the resistance to the motion of magnetic domain walls in the TbFeCo films at the interface of the magnetic layer and the seed or the cap layer because of the presence of pinning sites. As the roughness of the underlayer increases, more pinholes would be formed which prevent the motion of domain walls in TbFeCo

and hence the increase in coercivity. In our case the film grown on MgO substrate might have more pinning sites, which increased its coercivity.

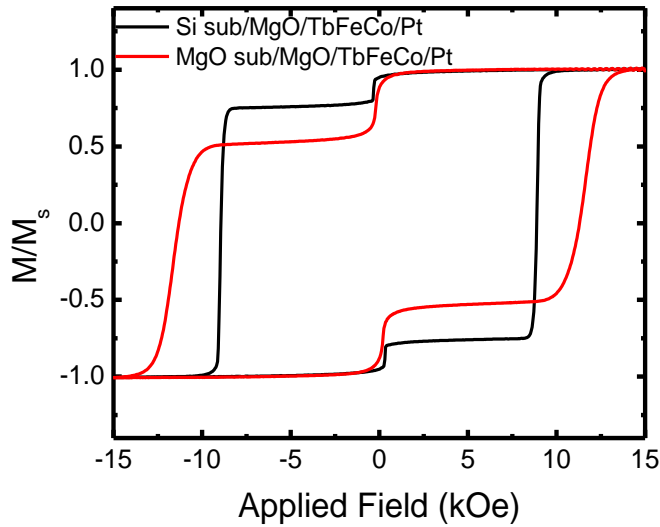


Figure 7.4: Out of plane M-H loops of TbFeCo grown on different seed layers.

The above films are in-situ annealed at 400C and the coercivity decreased dramatically for both the films after annealing as shown in figure 7.5. One of the reasons for decrease in coercivity of the films with increase in temperature is to do with the compensation temperature of these films. The compensation temperature is defined as the temperature where the total magnetization of the RE-TM alloy is zero; in other words, the magnetization of the Tb sublattice and FeCo sublattice is equal and opposite in magnitude and hence total magnetization is zero. In TbFeCo, usually below the compensation temperature the magnetization of the Tb sublattice is larger than the FeCo sublattice and vice versa. However, close to the compensation temperature, the magnetization is small and hence the demagnetization field is also small. Since the magnetization is very small or almost zero near the compensation temperature, the applied field has no handle to reverse the magnetization of the spin system, and hence the coercivity is large near the compensation temperature, which, for TbFeCo, is near room temperature. However, heating just a few degrees above the compensation temperature, gives a large reduction in coercivity.

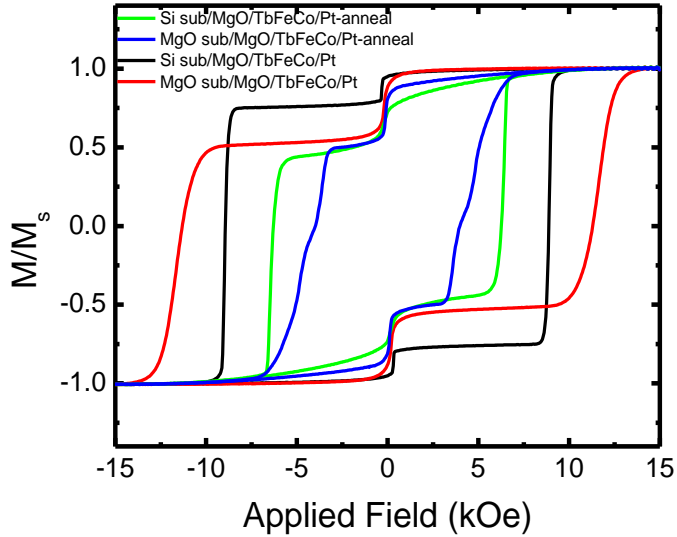


Figure 7.5: Annealing dependence on coercivity of TbFeCo films.

We have investigated different types of seed and cap layers such as SiO_2 , MgO, Pt and TiN on the coercivity and extent of oxidation of TbFeCo films. Si_3N_4 is used as a standard buffer layer above and below TbFeCo in magneto-optic storage disks: however, since it is not conductive, it may not be useful for MTJ devices. So we have tried a metallic nitride, for instance, TiN, which would be a good buffer layer for this application, in addition to having (001) texture that would be compatible with the MgO barrier layer. It is observed that the use of TiN under- and over- layers protects the TbFeCo film from oxidation. The kink which was believed to be because of the oxidation present in the previous samples is not present in the film with TiN under- and over- layers as shown in figure 7.6. Although the coercivity of TiN sandwiched TbFeCo film is still high, it is observed that the TiN layer is good for preventing oxidation.

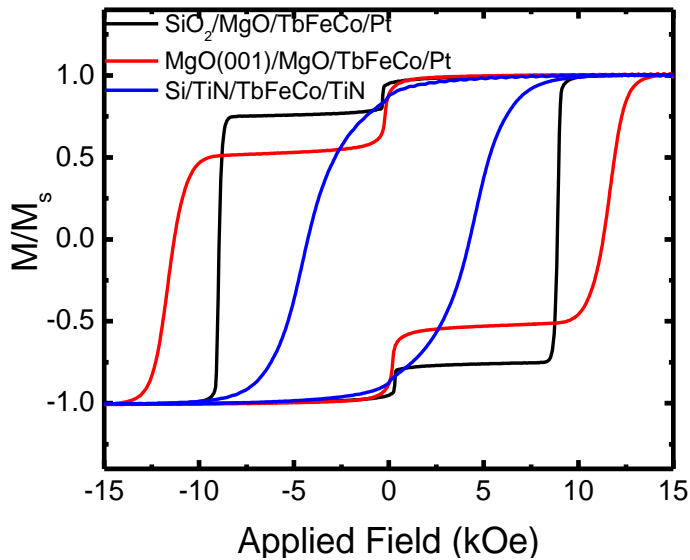


Figure 7.6: out of plane M-H loop of TbFeCo with different seed and cap layers.

7.6 Conclusions

In conclusion we report that TbFeCo films are highly susceptible to oxidation. In particular Tb reacts aggressively with O_2 , thereby degrading magnetic properties such as saturation magnetization as well as coercivity. It is observed that about 50nm of TbFeCo can pull the magnetization of 2nm of CoFeB films. These thicker CoFeB films adjacent to the MgO barrier layer are key to realizing high TMR, because of the symmetry filtering effect in CoFeB/MgO/CoFeB trilayer structure. Therefore, amorphous TbFeCo films which couple thicker CoFeB layers with (001) orientation and perpendicular magnetic anisotropy enhance the chance of obtaining higher TMR values. It is also observed that magnetic pinning sites play a crucial role in enhancing the coercivity of these films. These films when grown on different seed layers have different coercivities, mainly because of the magnetic pinning sites which impede the motion of a magnetic domain wall thereby delaying the magnetization reversal process.

VIII. Conclusions

In this dissertation, we have investigated a wide range of materials with magnetic anisotropy varying from in-plane to fully perpendicular: from Co-based multilayer stacks and Co- and Fe-based perpendicular alloys to amorphous TbFeCo. These materials herald a new generation of spintronics devices that can be integrated into conventional complementary metal-oxide semiconductor technology. These devices, when fully optimized, can be used in magnetic random access memory (MRAM), as well as spin transfer torque random access memory (STT-RAM) devices and also have potential applications in future spin-based quantum computer systems.

In chapter four and five of the dissertation we systematically studied various perpendicular magnetic anisotropy (PMA) magnetic multilayered systems. The multilayered systems we initially investigated include, Co/Pt, Fe/Pt, Fe/Pd, Co/Ni and Co/Pd. We have optimized the parameters such as bilayer thickness, bilayer ratio and number of bilayers to tune perpendicular magnetic anisotropy (PMA) as well as coercivity of Co/Ni ML's. We were able to grow Co/Ni out of plane anisotropy samples with various seed layers such as Ta/Pt and Ta/Cu. Although the out-of-plane anisotropy of these thin multilayers was mainly because of interfacial stress, as stated earlier, we found out that the seed layers on which these multilayers are grown are important as well. These multilayered stacks show good PMA when grown on Ta5/Pt10 nm seed layer as seen in figure 1(a) in chapter four, however, when similar stacks were grown on thicker Cu (50nm) layer the PMA was not good as indicated by MR loop seen in figure 5(b) in chapter 5. Ferromagnetic measurements were performed to obtain the effective magnetization

(M_{eff}) and damping parameter (α) values. Stress measurements indicated that the films are compressive as deposited and for a given total thickness, as the number of multilayers increased, the films became less compressive. Finally structural characterization was performed on these stacks showing that they have fcc (111) orientation with a very little interdiffusion.

A similar study was performed on Co/Pd multilayers. Parameters such as bilayer thickness, bilayer ratio and number of bilayers were optimized for the coercivity and out of plane anisotropy of these ML's. Co/Pd ferromagnetic resonance measurements were performed to obtain the M_{eff} and damping constant (α) values. A series of CoFeB thickness was deposited on top of these multilayered samples and the amount of CoFeB that can be pulled out of plane is predicted based on the FMR measurements. These multilayered combinations were used as free and pinned layers in magnetic tunnel junctions and excellent switching characteristics were seen. We have performed both field and current switching measurements on these devices. The TMR values obtained in case of field switching are about 10% at 100K which is very low as compared to conventional MgO-based in-plane MTJ's reported in the literature. We believe the fundamental problem in not obtaining TMR values greater than 10% is caused by the lattice mismatch between the fcc (111) PMA-ML's and MgO/CoFeB bcc (001) layers, combined with the necessarily thin (~0.5 nm) layers of CoFeB used in these junctions to maintain perpendicular anisotropy. The TMR values obtained with current switching is about 7.8 % on similar samples, however, the currents required to switch between parallel and antiparallel states of free and pinned layer was too high, so a bias field was applied during these measurements to assist current switching. We have also performed IETS measurements on these tunnel junctions to probe the MgO barrier layer quality and also to measure the characteristic spectra of the MgO

barrier layer by comparing with the calculated MgO phonon densities of states, electron energy loss spectra, and inelastic neutron scattering data.

In chapter six and seven of the dissertation, we have again investigated a different type of perpendicular magnetic anisotropy (PMA) materials, namely, $L1_0$ alloys and RE-TM alloys. $L1_0$ alloys were initially investigated for advanced media applications; however, due to their high thermal stability coupled with perpendicular magnetic anisotropy, these alloys were subsequently investigated for perpendicular magnetic tunnel junctions. We attempted $L1_0$ growth of $Fe_{50}Pd_{50}$, $Fe_{50}Pt_{50}$, $Co_{50}Pt_{50}$, and $Co_{50}Pd_{50}$. We tried various substrates, for instance, MgO (001) single crystal substrates pretreated to remove contaminants, a variety of seed layers, various deposition techniques such as the so-called “layer-by-layer growth” and various annealing techniques, both in-situ and ex-situ. However, except for the $Co_{50}Pd_{50}$ alloy, we could not achieve perpendicular magnetic anisotropy in any of these alloys. We have studied the effect of different seed layers, deposition temperature and the thickness of the $Co_{50}Pd_{50}$ alloy on the PMA and the $L1_0$ phase of the $Co_{50}Pd_{50}$ alloy. We observed perpendicular magnetic anisotropy in films greater than 20 nm thick, deposited between 400 and 500 °C. As the thickness of the CoPd alloy increased from 20 to 100nm, the PMA increased in these alloy films. Also, as the thickness increased the films showed increasingly slanted bow-tie shaped out of plane loops indicating multi-domain structures. It is also observed that the PMA of these alloys seems to be dependent on the annealing temperature: the films go from out of plane configuration to inplane configuration as the annealing temperature increases from 450C to 550C. Finally, it is observed that the PMA of the films is independent of the seed layer used; clearly indicating that out of plane anisotropy in these films is not because of the growth from the seed layer. XRD analysis shows that the films

grow with fcc (111) orientation and there is no (002) peak observed for these films, indicating that the films doesn't have any $L1_0$ phase.

We have also investigated perpendicular magnetic anisotropy (PMA) of rare earth transition metal (RE-TM) alloys which can be used for free and pinned layers in pMTJ's because of their tunable magnetic properties such as saturation magnetization and coercivity. We have studied the effect of seed and capping layers and annealing temperatures on magnetic properties of these films. It is observed that TbFeCo films are highly susceptible to oxidation. In particular Tb reacts aggressively with O_2 thereby degrading the magnetic properties such as saturation magnetization as well as coercivity. It is observed that about 50nm of TbFeCo can pull the magnetization of 2nm of CoFeB films out-of-plane. These thicker CoFeB films adjacent to the MgO barrier layer are key to realizing high TMR, because of the symmetry filtering effect in CoFeB/MgO/CoFeB trilayer structure. So, amorphous TbFeCo films which couple thicker CoFeB layers with (001) orientation and perpendicular magnetic anisotropy enhance the chance of obtaining higher TMR values. It was also believed that magnetic pinning sites play a crucial role in enhancing the coercivity of these films. These films when grown on different seed layers have different coercivities, mainly because of the magnetic pinning sites which impede the motion of a magnetic domain wall thereby delaying the magnetization reversal process.

In conclusion, this dissertation has explored a broad range of material systems with perpendicular magnetic anisotropy for application in magnetic tunnel junctions utilized in spin-torque transfer random access memory. We have confirmed or newly discovered many of the fundamental characteristics that induce perpendicular magnetic anisotropy, and gained a deep understanding of the challenges ahead to achieve optimized TMR, thermal stability and switching currents. Future work based on our findings will be able to optimize these properties to

achieve magnetic tunnel junctions that will make STT-RAM a viable option for high density memory.

IX. References

- 1) W. J. Gallagher and S. S. P. Parkin, *IBM J. Res. & Dev.* 50, 5–23 (2006).
- 2) Thomson, W, *Proc. Roy. SOC.* 8, 546-550 (1857).
- 3) Ramirez, A.P., *Journal of Physics-Condensed Matter*, 9 (39), 8171-8199 (1997).
- 4) N. Garcia, M. Munoz, and Y.W. Zhao, *Phys. Rev. Lett.* 82, 2923-2926 (1999).
- 5) M. N. Baibich, J. M. Broto, A. Fert, F. Nguyen Van Dau, F. Petroff, P. Etienne, G. Creuzet, A. Friederich, and J. Chazelas, *Phys. Rev. Lett.* 61, 2472–2475 (1988).
- 6) P. Grunberg, R. Schreiber, Y. Pang, M. B. Brodsky, and H. Sowers, *Phys. Rev. Lett.* 57, 2442–2445 (1986).
- 7) G. Binasch, P. Grunberg, F. Saurenbach, and W. Zinn, *Phys. Rev. B.* 39, 4828–4830 (1989).
- 8) S. S. P. Parkin, S. Fan, N. More, and K. P. Roche, *J. Appl. Phys.* 67, 5931 (1990).
- 9) B. Dieny, V. S. Speriosu, S. S. P. Parkin, B. A. Gurney, D. R. Whilhoit, and D. Mauri, *Phys. Rev. B.* 43, 1297–1300 (1991).
- 10) S. S. P. Parkin, Z. G. Li, and D. J. Smith, *Appl. Phys. Lett.* 58, 2710–2712 (1991).
- 11) S. S. P. Parkin, N. More and K. P. Roche, *Phys. Rev. Lett.* 64, 2304–2307 (1990).
- 12) S. S. P. Parkin, R. Bhadra and K. P. Roche, *Phys. Rev. Lett.* 66, 2152–2155 (1991).
- 13) W. H. Meiklejohn and C. P. Bean, *Phys. Rev.* 102, 1413–1414 (1956).
- 14) W. H. Meiklejohn and C. P. Bean, *Phys. Rev.* 105, 904–913 (1957).
- 15) *Proc. R. Soc. Lond. A*, 156, August 17, 368-382 (1936).
- 16) S. Yuasa and D. D. Djayaprawira, *J. Phys. D: Appl. Phys.* 40, 337–354 (2007).
- 17) M. Julliere, *Phys. Lett. A.* 54, 225 (1975).

- 18) P. M. Tedrow and R. Meservey, *Phys. Rev. B.* 7, 318 (1973).
- 19) R. Meservey and P. M. Tedrow, *Phys. Rep.* 238, 173 (1994).
- 20) T. Miyazaki and N. Tezuka, *J. Magn. Magn. Mater.* 139, L231 (1995).
- 21) J. S. Moodera, L. R. Kinder, T. M. Wong and R. Meservey, *Phys. Rev. Lett.* 74, 3273 (1995).
- 22) W. H. Butler, X. G. Zhang, T. C. Schulthess and J. M. MacLaren, *Phys. Rev. B.* 63, 054416 (2001).
- 23) S. S. P. Parkin, C. Kaiser, A. Panchula, P. M. Rice, B. Hughes, M. Samant, S. H. Yang, *Nature Materials*, 3(12), 862-867 (2004).
- 24) S. Yuasa, T. Nagahama, A. Fukushima, Y. Suzuki and K. Ando, *Nature Materials*, 3(12), 868-871 (2004).
- 25) D. D. Djayaprawira, Tsunekawa, K. Naga, M. Maehara, H. Yamagata, S. Watanabe, N. Yuasa, S. Suzuki and Y. Ando, *Appl. Phys. Lett.* 86(9), 092502 (2005).
- 26) J. C. Slonczewski, *J. Magn. Magn. Mater.* 159, 1 (1996).
- 27) L. Berger, *Phys. Rev. B.* 54, 9353 (1996).
- 28) M. Tsoi, A. G. Jansen, J. Bass, W. C. Chiang, M. Seck, V. Tsoi, P. Wyder, *Phys. Rev. Lett.* 81 (2) 493 (1998).
- 29) J. A. Katine, F. J. Albert, R. A. Buhrman, E. B. Myers, D. C. Ralph, *Phys. Rev. Lett.* 84 (14) 3149 (2000).
- 30) X. Zhu and J. G. Zhu, *IEEE Trans. Magn.*, 42, 2739–2741 (2006).
- 31) M. Hosomi, H. Yamagishi, T. Yamamoto, K. Bessho, Y. Higo, K. Yamane, H. Yamada, M. Shoji, H. Hachino, C. Fukumoto, H. Nagao, and H. Kano, *IEDM Tech. Dig.* 459–462 (2005).
- 32) T. Kawahara, *ISSCC Dig. Tech. Papers* 480–481(2007).

- 33) N. Nishimura, T. Hirai, A. Koganei, T. Ikeda, K. Okano, Y. Sekiguchi, and Y. Osada, *J. Appl. Phys.* 91, 5246 (2002).
- 34) M. Nakayama, T. Kai, N. Shimomura, M. Amano, E. Kitagawa, T. Nagase, M. Yoshikawa, T. Kishi, S. Ikegawa, and H. Yoda, *J. Appl. Phys.* 103, 07A710 (2008).
- 35) H. Ohmori, T. Hatori, and S. Nakagawa, *J. Appl. Phys.* 103, 07A911 (2008).
- 36) S. Mitani, K. Tsukamoto, T. Seki, T. Shima, and K. Takanashi, *IEEE Trans. Magn.* 41, 2606 (2005).
- 37) M. Yoshikawa, E. Kitagawa, T. Nagase, T. Daibou, M. Nagamine, K. Nishiyama, T. Kishi, and H. Yoda, *IEEE Trans. Magn.* 44, 2573 (2008).
- 38) G. Kim, Y. Sakuraba, M. Oogane, Y. Ando, and T. Miyazaki, *Appl. Phys. Lett.* 92, 172502 (2008).
- 39) S. H. Kang, *JOM Journal of the minerals, Metals and Materials Society.* 60, (9), 28-33 (2008).
- 40) S. M. Thompson, *J. Phys. D: Appl. Phys.* 41, 093001 (2008).
- 41) J. A. Katine, F. J. Albert, R. A. Buhrman, E. B. Myers, and D. C. Ralph, *Phys. Rev. Lett.* 84, 3149 (2000).
- 42) S. Mangin, D. Ravelosona, J. A. Katine, M. J. Carey, B. D. Terris, and E. E. Fullerton, *Nat. Mater.*, 5, 210–215 (2006).
- 43) D. Chiba, Y. Sato, T. Kita, F. Matsukura, and H. Ohno, *Phys. Rev. Lett.* 93, 216602 (2004).
- 44) P. M. Braganca, I. N. Krivorotov, O. Ozatay, A. G. F. Garcia, N. C. Emley, J. C. Sankey, D. C. Ralph, and R. A. Buhrman, *Appl. Phys. Lett.* 87, 112507 (2005).

- 45) O. Ozatay, P. G. Gowtham, K. W. Tan, J. C. Read, K. A. Mkhoyan, M. G. Thomas, G. D. Fuchs, P. M. Braganca, E. M. Ryan, K. V. Thadani, J. Silcox, D. C. Ralph, and R. A. Buhrman, *Nature Mater.* 7, 567 (2008).
- 46) Z. Diao, Z. Li, S. Wang, Y. Ding, A. Panchula, E. Chen, L. -C. Wang, and Y. Huai, *J. Phys.: Condens. Matter* 19, 165209 (2007).
- 47) F. J. A. den Broeder, E. Janssen, W. Hoving and W. B. Zeper, *IEEE Trans. Magn.* 28, (5), (1992).
- 48) G. H. O. Daalderop, P. J. Kelly, and M. F. H. Schuurmans, *Phys. Rev. B.* 42, (11), (1990).
- 49) G. H. O. Daalderop, P. J. Kelly, and F. J. A. den Broeder, *Phys. Rev. Lett.* 68, (5), (1992).
- 50) C. Kittel, *Phys. Rev.* 73, 155-161 (1948).
- 51) R. Sbiaa, C. Z. Hua, S. N. Piramanayagam, R. Law, K. O. Aung, and N. Thiyagarajah, *J. Appl. Phys.* 106, 023906, (2009).
- 52) B. J. Kirby, S. M. Watson, J. E. Davies, G. T. Zimanyi, K. Liu, R. D. Shull, and J. A. Borchers, *J. Appl. Phys.* 105, 07C929, (2009).
- 53) S. Mohanan, M. Smetanin, J. Weissmüller and U. Herr, *Scripta Materialia*, 60, 756–759, (2009).
- 54) S. Nakagawa, H. Yoshikawa, *J. Magn. Mater.* 287, 193–198 (2005).
- 55) F. Garcia, G. Casali, S. Auffret, B. Rodmacq, and B. Dieny, *J. Appl. Phys.* 91, 6905–6907, (2002).
- 56) S. D. Kim, D. Lim, and S.-R. Lee, *Phys. Stat. Sol. (a)*, 201, 1666–1669, (2004).
- 57) S. D. Choi, H. W. Joo, D. K. Yun, M. S. Lee, K. A. Lee, H. S. Lee, S. W. Kim, S. S. Lee, and D. G. Hwang, *J. Magn. Mater.* 11, 70–73, (2006).
- 58) D. Lim, K. Kim, S. Kim, W. Y. Jeung, and S. R. Lee, *IEEE Trans. Magn.* 45, 2407, (2009)

- 59) D. Lim, S. Kim, S. R. Lee, *J. Appl. Phys.* 97, 10C902 (2005).
- 60) B. Heinrich, J. F. Cochran and R. Hasegawa, *J. Appl. Phys.* 57, 3690, (1985).
- 61) H. Lee, L. Wen, M. Pathak, P. Janssen, P. LeClair, C. Alexander, C. K. A. Mewes and T. Mewes, *J. Phys. D: Appl. Phys.* 41, 215001, (2008).
- 62) G. Hu, T. Thomson, C. T. Rettner, S. Raoux and B. D. Terris, *J. Appl. Phys.* 97, 10J702 (2005).
- 63) Z. R. Tadisina, A. Natarajarathinam, B. D. Clark, A. L. Highsmith, T. Mewes, S. Gupta, E. Chen and S. Wang, *J. Appl. Phys.* (In Press).
- 64) M. T. Johnson, P. J. H. Bloemen, F. J. A. den Broeder, and J. J. de Vries, *Rep. Prog. Phys.* 59, 1409 (1996).
- 65) J. H. Park, C. Park, T. Jeong, M. T. Moneck, N. T. Nufer, and J. G. Zhu, *J. Appl. Phys.* 103, 07A917, (2008).
- 66) S. Okamoto, N. Kikuchi, O. Kitakami, T. Miyazaki, Y. Shimada and K. Fukamichi, *Phys. Rev. B.* 66, 024413 (2002).
- 67) A. Martins, M. C. A. Fantini, N. M. Souza-Neto, A. Y. Ramos, A. D. Santos, *J. Magn. Magn. Mater.* 305, 152–156, (2006).
- 68) E. M. Artem'ev* and M. E. Artem'ev, *JETP Letters*, 86, (11), 727–729 (2007).
- 69) J. Kim, K. Barmak, M. De Graef, L. H. Lewis and D. C. Crew, *J. Appl. Phys.* 87, (91), (2000).
- 70) T. Rahman, X. Liu, A. Morisako, and M. Matsumoto, *J. Magn. Magn. Mater.* 287, 250–254 (2005).
- 71) S. Miyanishi, K. Kojima, J. Sato, K. Takayama, H. Fuji, A. Takahashi and K. Ohta, *J. Appl. Phys.* 93, 7801 (2003).

- 72) H. Ito, K. Song, and M. Naoe, *J. Appl. Phys.* 79, (8), 6273–6275 (1996).
- 73) J. Sato, Y. Murakami, H. Fuji, K. Kojima, A. Takahashi, R. Nakatani, and M. Yamamoto, *Jpn. J. Appl. Phys.* 47, (1), 150–153 (2008).
- 74) Y. H. Fang, P. C. Kuo, C. Y. Chou, S. C. Chen, N. W. Cheng, and P.L. Lin, *J. Magn. Magn. Mater.* 310, e930–e932 (2007).
- 75) M. T. Rahman, X. Liu, and A. Morisako, *J. Magn. Magn. Mater.* 303, 133–e136 (2006).
- 76) H. Katayama, M. Hamamoto, J. Sato, Y. Murakami, and K. Kojima, “New developments in laser-assisted magnetic,” *IEEE Trans. Magn.* 1. 36, (1), (2000).
- 77) S. Takayama, T. Niihara, K. Kaneko, Y. Sugita, M. Ojima, *J. Appl. Phys.* 61, 2610 (1987).
- 78) M. Takahashi, T. Niihara, N. Ohta, *J. Appl. Phys.* 64, 262 (1988).